

Interrogating theoretical models of neural computation with deep inference

Sean R. Bittner, Agostina Palmigiano, Alex T. Piet, Chunyu A. Duan, Carlos D. Brody,
Kenneth D. Miller, and John P. Cunningham.

¹ 1 Abstract

² The cornerstone of theoretical neuroscience is the circuit model: a system of equations that captures
³ a hypothesized neural mechanism. Such models are valuable when they give rise to an experimen-
⁴ tally observed phenomenon – whether behavioral or in terms of neural activity – and thus can offer
⁵ insights into neural computation. The operation of these circuits, like all models, critically depends
⁶ on the choices of model parameters. Historically, the gold standard has been to analytically derive
⁷ the relationship between model parameters and computational properties. However, this enterprise
⁸ quickly becomes infeasible as biologically realistic constraints are included into the model increas-
⁹ ing its complexity, often resulting in *ad hoc* approaches to understanding the relationship between
¹⁰ model and computation. We bring recent machine learning techniques – the use of deep generative
¹¹ models for probabilistic inference – to bear on this problem, learning distributions of parameters
¹² that produce the specified properties of computation. Importantly, the techniques we introduce
¹³ offer a principled means to understand the implications of model parameter choices on compu-
¹⁴ tational properties of interest. We motivate this methodology with a worked example analyzing
¹⁵ sensitivity in the stomatogastric ganglion. We then use it to generate insights into neuron-type
¹⁶ input-responsivity in a model of primary visual cortex, a new understanding of rapid task switch-
¹⁷ ing in superior colliculus models, and attribution of bias in recurrent neural networks solving a toy
¹⁸ mathematical problem. More generally, this work offers a quantitative grounding for theoretical
¹⁹ models going forward, pointing a way to how rigorous statistical inference can enhance theoretical
²⁰ neuroscience at large.

²¹ 2 Introduction

²² The fundamental practice of theoretical neuroscience is to use a mathematical model to understand
²³ neural computation, whether that computation enables perception, action, or some intermediate
²⁴ processing [1]. In this field, a neural computation is systematized with a set of equations – the
²⁵ model – and these equations are motivated by biophysics, neurophysiology, and other conceptual
²⁶ considerations. The function of this system is governed by the choice of model parameters, which

when configured appropriately, give rise to a measurable signature of a computation. The work of analyzing a model then requires solving the inverse problem: given a computation of interest, how can we reason about these suitable parameter configurations? The inverse problem is crucial for reasoning about likely parameter values, uniquenesses and degeneracies, attractor states and phase transitions, and predictions made by the model.

Consider the idealized practice: one carefully designs a model and analytically derives how model parameters govern the computation. Seminal examples of this gold standard include our field’s understanding of memory capacity in associative neural networks [2] and chaos and autocorrelation timescales in random neural networks [3] (adopting approaches from physics), and the paradoxical effect [4] and decision making [5] in rate models. Unfortunately, as circuit models include more biological realism, theory via analytic derivation becomes intractable. This creates an unfavorable tradeoff. On the one hand, one may tractably analyze systems of equations with unrealistic assumptions (for example symmetry or gaussianity), producing accurate inferences about parameters of a too-simple model. On the other hand, one may choose a more biologically accurate, scientifically relevant model at the cost of *ad hoc* approaches to analysis (simply examining simulated activity), potentially resulting in bad inferences and thus erroneous scientific predictions and conclusions.

Of course, this same tradeoff has been confronted in many scientific fields and engineering problems characterized by the need to do inference in complex models. In response, the machine learning community has made remarkable progress in recent years, via the use of deep neural networks as a powerful inference engine: a flexible function family that can map observed phenomena (in this case the measurable signal of some computation) back to probability distributions quantifying the likely parameter configurations. One celebrated example of this approach from machine learning, of which we draw key inspiration for this work, is the variational autoencoder [6, 7], which uses a deep neural network to induce an (approximate) posterior distribution on hidden variables in a latent variable model, given data. Indeed, these tools have been used to great success in neuroscience as well, in particular for interrogating parameters (sometimes treated as hidden states) in models of both cortical population activity [8, 9, 10, 11] and animal behavior [12, 13, 14]. These works have used deep neural networks to expand the expressivity and accuracy of statistical models of neural data [15].

However, these inference tools have not significantly influenced the study of theoretical neuroscience models, for at least three reasons. First, at a practical level, the nonlinearities and dynamics of many theoretical models are such that conventional inference tools typically produce a narrow set of

59 insights into these models. Indeed, only in the last few years has deep learning research advanced to
60 a point of relevance to this class of problem. Second, the object of interest from a theoretical model
61 is not typically data itself, but rather a qualitative phenomenon – inspection of model behavior, or
62 better, a measurable signature of some computation – an *emergent property* of the model. Third,
63 because carefully constructed biological models do not fit cleanly into the framing of a statistical
64 model. Technically, because many such models stipulate a noisy system of differential equations
65 that can only be sampled or realized through forward simulation, they lack the explicit likelihood
66 and priors central to the probabilistic modeling toolkit.

67 To address these three challenges, we developed an inference methodology – ‘emergent property
68 inference’ – which learns a distribution over parameter configurations in a theoretical model. This
69 distribution has two critical properties: *(i)* it is chosen such that draws from the distribution (pa-
70 rameter configurations) correspond to systems of equations that give rise to a specified emergent
71 property (a set of constraints); and *(ii)* it is chosen to have maximum entropy given those con-
72 straints, such that we identify all likely parameters and can use the distribution to reason about
73 parametric sensitivity and degeneracies [16]. First, we stipulate a bijective deep neural network that
74 induces a flexible family of probability distributions over model parameterizations with a probabil-
75 ity density we can calculate [17, 18, 19]. Second, we quantify the notion of emergent properties as a
76 set of moment constraints on datasets generated by the model. Thus, an emergent property is not a
77 single data realization, but a phenomenon or a feature of the model, which is ultimately the object
78 of interest in theoretical neuroscience. Conditioning on an emergent property requires a variant of
79 deep probabilistic inference methods, which we have previously introduced [20]. Third, because we
80 cannot assume the theoretical model has explicit likelihood on data or the emergent property of
81 interest, we use stochastic gradient techniques in the spirit of likelihood free variational inference
82 [21]. Taken together, emergent property inference (EPI) provides a methodology for inferring pa-
83 rameter configurations consistent with a particular emergent phenomena in theoretical models. We
84 use a classic example of parametric degeneracy in a biological system, the stomatogastric ganglion
85 [22], to motivate and clarify the technical details of EPI.

86 Equipped with this methodology, we then investigated three models of current importance in the-
87 oretical neuroscience. These models were chosen to demonstrate generality through ranges of bi-
88 ological realism (from conductance-based biophysics to recurrent neural networks), neural system
89 function (from pattern generation to abstract cognitive function), and network scale (from four to
90 infinite neurons). First, we use EPI to produce a set of verifiable hypotheses of input-responsivity

in a four neuron-type dynamical model of primary visual cortex; we then validate these hypotheses in the model. Second, we demonstrated how the systematic application of EPI to levels of task performance can generate experimentally testable hypotheses regarding connectivity in superior colliculus. Third, we use EPI to uncover the sources of bias in a low-rank recurrent neural network executing a toy mathematical computation. The novel scientific insights offered by EPI contextualize and clarify the previous studies exploring these models [23, 24, 25, 26] and more generally, suggests a departure from realism vs tractability considerations towards the use of modern machine learning for sophisticated interrogation of biologically relevant models.

We note that, during our preparation and early presentation of this work [27, 28], another work has arisen with broadly similar goals: bringing statistical inference to mechanistic models of neural circuits [29]. We are excited by this broad problem being recognized by the community, and we emphasize that these works offer complementary neuroscientific contributions and use different technical methodologies. While we have advanced our research on deep generative modeling [20] to a point of significant relevance to statistical inference in theoretical neuroscience, they have also furthered their research on approximate Bayesian inference in such models [30]. The existence of these complementary methodologies emphasizes the increased importance and timeliness of both works.

3 Results

3.1 Motivating emergent property inference of theoretical models

Consideration of the typical workflow of theoretical modeling clarifies the need for emergent property inference. First, one designs or chooses an existing model that, it is hypothesized, captures the computation of interest. To ground this process in a well-known example, consider the stomatogastric ganglion (STG) of crustaceans, a small neural circuit which generates multiple rhythmic muscle activation patterns for digestion [31]. Despite full knowledge of STG connectivity and a precise characterization of its rhythmic pattern generation, biophysical models of the STG have complicated relationships between circuit parameters and neural activity [22, 32]. A model of the STG [23] is shown schematically in Figure 1A, and note that the behavior of this model will be critically dependent on its parameterization – the choices of conductance parameters $z = [g_{el}, g_{synA}]$. Specifically, the two fast neurons ($f1$ and $f2$) mutually inhibit one another, and oscillate at a faster frequency than the mutually inhibiting slow neurons ($s1$ and $s2$), and the hub neuron (hub) couples



Figure 1: Emergent property inference (EPI) in the stomatogastric ganglion. A. For a choice of model (STG) and emergent property (network syncing), emergent property inference (EPI, gray box) learns a distribution of the model parameters $z = [g_{el}, g_{synA}]$ producing network syncing. In the STG model, jagged connections indicate electrical coupling having electrical conductance g_{el} . Other connections in the diagram are inhibitory synaptic projections having strength g_{synA} onto the hub neuron, and $g_{synB} = 5\text{nS}$ for mutual inhibitory connections. Network syncing traces are colored by log probability of their generating parameters in the EPI-inferred distribution. B. An EPI distribution of STG model parameters producing network syncing. Samples are colored by log density. Distribution contours of emergent property value error are shown at levels of 2×10^{-6} , 2×10^{-5} , and 2×10^{-4} . Eigenvectors of the Hessian at the mode of the inferred distribution are indicated as v_1 and v_2 . Simulated activity is shown for three samples (stars). (Inset) Sensitivity of the system with respect to network syncing along all dimensions of parameter space away from the mode. (see Section A.2.1). C. Deep probability distributions map a latent random variable w through a deep neural network with weights and biases θ to parameters $z = f_\theta(w)$ distributed as $q_\theta(z)$. D. EPI optimization: To learn the EPI distribution $q_\theta(z)$ of model parameters that produce an emergent property, the emergent property statistics $T(x)$ are set in expectation over model parameter samples $z \sim q_\theta(z)$ and model simulations $x \sim p(x | z)$ to emergent property values μ . The maximum entropy distribution producing the emergent property.

121 with the fast or slow population or both.

122 Second, once the model is selected, one defines the emergent property, the measurable signal of
 123 scientific interest. To continue our running STG example, one such emergent property is the
 124 phenomenon of *network syncing* – in certain parameter regimes, the frequency of the hub neuron
 125 matches that of the fast and slow populations at an intermediate frequency. This emergent property
 126 is shown in Figure 1A at a frequency of 0.54Hz.

127 Third, qualitative parameter analysis ensues: since precise mathematical analysis is intractable in
 128 this model, a brute force sweep of parameters is done [23]. Subsequently, a qualitative description
 129 is formulated to describe the different parameter configurations that lead to the emergent property.
 130 In this last step lies the opportunity for a precise quantification of the emergent property as a
 131 statistical feature of the model. Once we have such a methodology, we can infer a probability
 132 distribution over parameter configurations that produce this emergent property.

133 Before presenting technical details (in the following section), let us understand emergent property
 134 inference schematically: EPI (Fig. 1A gray box) takes, as input, the model and the specified
 135 emergent property, and as its output, produces the parameter distribution shown in Figure 1B.
 136 This distribution – represented for clarity as samples from the distribution – is then a scientifically
 137 meaningful and mathematically tractable object. In the STG model, this distribution can be
 138 specifically queried to reveal the prototypical parameter configuration for network syncing (the
 139 mode; Figure 1B yellow star), and how network syncing decays based on changes away from the
 140 mode. Intuitively, the probability density of the samples is in agreement with the emergent property
 141 value error (Fig. 1B contours). Furthermore, the eigenvectors of the distribution Hessian at the
 142 mode can be queried to quantitatively formalize the robustness of network syncing (Fig. 1B v_1 and
 143 v_2). Indeed, samples equidistant from the mode along these EPI-identified dimensions of sensitivity
 144 (v_1) and degeneracy (v_2) have diminished or preserved network syncing, respectively (Figure 1B
 145 inset and activity traces). Further validation of EPI is available in the supplementary materials,
 146 where we analyze a simpler model for which ground-truth statements can be made (Section A.1.1).

147 3.2 A deep generative modeling approach to emergent property inference

148 Emergent property inference (EPI) systematizes the three-step procedure of the previous section.
 149 First, we consider the model as a coupled set of differential (and potentially stochastic) equations
 150 [23]. In the running STG example, its activity $x = [x_{f1}, x_{f2}, x_{hub}, x_{s1}, x_{s2}]$ is the membrane potential

151 for each neuron, which evolves according to the biophysical conductance-based equation:

$$C_m \frac{dx}{dt} = -h(x; z) = -[h_{leak}(x; z) + h_{Ca}(x; z) + h_K(x; z) + h_{hyp}(x; z) + h_{elec}(x; z) + h_{syn}(x; z)] \quad (1)$$

152 where $C_m=1\text{nF}$, and h_{leak} , h_{Ca} , h_K , h_{hyp} , h_{elec} , h_{syn} are the leak, calcium, potassium, hyperpolarization, electrical, and synaptic currents, all of which have their own complicated dependence on x and $z = [g_{el}, g_{synA}]$ (see Section A.2.1).

155 Second, we define the emergent property, which as above is network syncing: oscillation of the
 156 entire population at an intermediate frequency of our choosing (Figure 1A bottom). Quantifying
 157 this phenomenon is straightforward: we define network syncing to be that each neuron’s spiking
 158 frequency – denoted $\omega_{f1}(x)$, $\omega_{f2}(x)$, etc. – is close to an intermediate frequency of 0.54Hz. Mathematically,
 159 we achieve this via constraints on the mean and variance of $\omega_i(x)$ for each neuron
 160 $i \in \{f1, f2, \text{hub}, s1, s2\}$, and thus:

$$\mathbb{E}[T(x)] \triangleq \mathbb{E} \begin{bmatrix} \omega_{f1}(x) \\ \vdots \\ (\omega_{f1}(x) - 0.54)^2 \\ \vdots \end{bmatrix} = \begin{bmatrix} 0.54 \\ \vdots \\ 0.025^2 \\ \vdots \end{bmatrix} \triangleq \mu, \quad (2)$$

161 which completes the quantification of the emergent property.

162 Third, we perform emergent property inference: we find a distribution over parameter configura-
 163 tions z , and insist that samples from this distribution produce the emergent property; in other
 164 words, they obey the constraints introduced in Equation 2. This distribution will be chosen from
 165 a family of probability distributions $\mathcal{Q} = \{q_\theta(z) : \theta \in \Theta\}$, defined by a deep generative distribution
 166 of the normalizing flow class [17, 18, 19] – neural networks which transform a simple distribution
 167 into a suitably complicated distribution (as is needed here). This deep distribution is represented
 168 in Figure 1C (and see Methods for more detail). Then, mathematically, we must solve the following
 169 optimization program:

$$\begin{aligned} & \underset{q_\theta \in \mathcal{Q}}{\operatorname{argmax}} H(q_\theta(z)) \\ & \text{s.t. } \mathbb{E}_{z \sim q_\theta} [\mathbb{E}_{x \sim p(x|z)} [T(x)]] = \mu, \end{aligned} \quad (3)$$

170 where $T(x), \mu$ are defined as in Equation 2, and $p(x|z)$ is the intractable distribution of data from
 171 the model (x), given that model’s parameters z (we access samples from this distribution by running
 172 the model forward). The purpose of each element in this program is detailed in Figure 1D. Finally,

we recognize that many distributions in \mathcal{Q} will respect the emergent property constraints, so we require a normative principle to select amongst them. This principle is captured in Equation 3 by the primal objective H . Here we chose Shannon entropy as a means to find parameter distributions with minimal assumptions beyond some chosen structure [33, 34, 20, 35], but we emphasize that the EPI method is unaffected by this choice (but the results of course will depend on the primal objective chosen).

EPI optimizes the weights and biases θ of the deep neural network (which induces the probability distribution) by iteratively solving Equation 3. The optimization is complete when the sampled models with parameters $z \sim q_\theta$ produce activity consistent with the specified emergent property. Such convergence is evaluated with a hypothesis test that the mean of each emergent property statistic is not different than its emergent property value (see Section A.1.2). Equipped with this method, now prove out the value of EPI by using it to investigate and produce novel insights about three prominent models in neuroscience.

3.3 Comprehensive input-responsivity in a nonlinear sensory system

Dynamical models of excitatory (E) and inhibitory (I) populations with supralinear input-output function have succeeded in explaining a host of experimentally documented phenomena. In a regime characterized by inhibitory stabilization of strong recurrent excitation, these models gives rise to paradoxical responses [4], selective amplification [36], surround suppression [37] and normalization [38]. Despite their strong predictive power, E-I circuit models rely on the assumption that inhibition can be studied as an indivisible unit. Instead, experimental evidence shows that inhibition is composed of distinct elements (parvalbumin (P), somatostatin(S), vip (V)) composing 80% of GABAergic interneurons in V1 [39, 40, 41] and that these inhibitory cell types follow specific connectivity patterns (Fig. 2A) [42]. Recent theoretical advances [24, 43, 44], have only started to address the consequences of this multiplicity in the dynamics of V1, strongly relying on linear theoretical tools. Here, we use EPI to go beyond linear theory by systematically generating and evaluating hypotheses of circuit model function using distributions of parameters producing various neuron-type population responses.

Specifically, we consider a four-dimensional circuit model with dynamical state given by the firing rate x of each neuron-type population $x = [x_E, x_P, x_S, x_V]^\top$. Given a time constant of $\tau = 20$ ms and a power $n = 2$, the dynamics are driven by the rectified ($\|\cdot\|_+$) and exponentiated sum of recurrent (Wx) and external h inputs:



Figure 2: Hypothesis generation through EPI in a V1 model. A. Four-population model of primary visual cortex with excitatory (black), parvalbumin (blue), somatostatin (red), and vip (green) neurons. Some neuron-types largely do not form synaptic projections to others (excitatory and inhibitory projections filled and unfilled, respectively). B. V1 model simulations for input (solid) $h = b$ and (dashed) $h = b + dh$. Stars indicate the linear response prediction. C. EPI distributions on differential input dh conditioned on differential response $\mathcal{B}(\alpha, y)$. Supporting evidence for the four generated hypotheses are indicated by gray boxes with labels H1, H2, H3, and H4. The linear prediction from two standard deviations away from y (from negative to positive) is overlaid in magenta (very small, near origin).

$$\tau \frac{dx}{dt} = -x + [Wx + h]_+^n \quad (4)$$

- 204 The effective connectivity weights W were obtained from experimental recordings of publicly avail-
 205 able datasets of mouse V1 [45, 46] (see Section A.2.2). The input $h = b + dh$ is comprised of
 206 a baseline input $b = [b_E, b_P, b_S, b_V]^\top$ and a differential input $dh = [dh_E, dh_P, dh_S, dh_V]^\top$ to each
 207 neuron-type population. Throughout subsequent analyses, the baseline input is $b = [1, 1, 1, 1]^\top$.
 208 With this model, we are interested in the differential responses of each neuron-type population to
 209 changes in input dh . Initially, we studied the linearized response of the system to input $\frac{dx_{ss}}{dh}$ at the
 210 steady state response x_{ss} , i.e. a fixed point. All analyses of this model consider the steady state
 211 response, so we drop the notation ss from here on. While this linearization accurately predicts
 212 differential responses $dx = [dx_E, dx_P, dx_S, dx_V]$ for small differential inputs to each population
 213 $dh = [0.1, 0.1, 0.1, 0.1]$ (Fig 2B left), the linearization is a poor predictor in this nonlinear model
 214 more generally (Fig. 2B right). Currently available approaches to deriving the steady state response
 215 of the system are limited.
 216 To get a more comprehensive picture of the input-responsivity of each neuron-type beyond linear
 217 theory, we used EPI to learn a distribution of the differential inputs to each population dh that
 218 produce an increase of $y \in \{0.1, 0.5\}$ in the rate of each neuron-type population $\alpha \in \{E, P, S, V\}$.
 219 We want to know the differential inputs dh that result in a differential steady state dx_α (the change
 220 in x_α when receiving input $h = b + dh$ with respect to the baseline $h = b$) of value y with some small,
 221 arbitrarily chosen amount of variance 0.01². These statements amount to the emergent property

$$\mathcal{B}(\alpha, y) \triangleq \mathbb{E} \begin{bmatrix} dx_\alpha \\ (dx_\alpha - y)^2 \end{bmatrix} = \begin{bmatrix} y \\ 0.01^2 \end{bmatrix} \quad (5)$$

- 222 We maintain the notation $\mathcal{B}(\cdot)$ throughout the rest of the study as short hand for emergent prop-
 223 erty, which represents a different signature of computation in each application. In each column
 224 of Figure 2C visualizes the inferred distribution, available through EPI, of dh corresponding to
 225 an excitatory (red), parvalbumin (blue), somatostatin (red) and vip (green) neuron-type increase,
 226 while each row corresponds to amounts of increase 0.1 and 0.5. For each pair of parameters we
 227 show the two-dimensional marginal distribution of samples colored by $\log q_\theta(dh \mid \mathcal{B}(\alpha, y))$. The
 228 inferred distributions immediately suggest four hypotheses:
 229

- 230 H1: as is intuitive, each neuron-type's firing rate should be sensitive to that neuron-type's

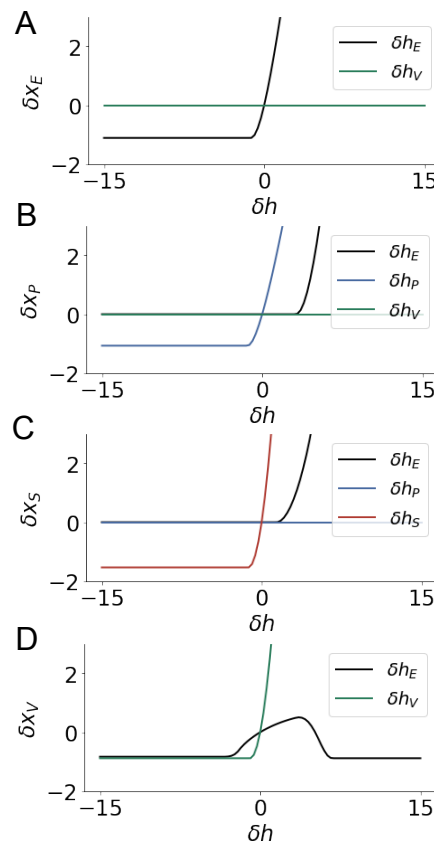


Figure 3: Confirming EPI generated hypotheses in V1. A. Differential responses by the E-population to changes in individual input $\delta h_\alpha \hat{u}_\alpha$ away from the mode of the EPI distribution dh^* . B-D Same plots for the P-, S-, and V-populations. Labels H1, H2, H3, and H4 indicate which curves confirm which hypotheses.

direct input (e.g. Fig. 2C H1 gray box indicates low variance in dh_E when $\alpha = E$. Same observation in all inferred distributions);
 H2: the E- and P-populations should be largely unaffected by input to the V-population (Fig. 2C H2 gray boxes indicate high variance in dh_V when $\alpha \in \{E, P\}$);
 H3: the S-population should be largely unaffected by input to the P-population (Fig. 2C H3 gray boxes indicate high variance in dh_P when $\alpha = S$);
 H4: there should be a nonmonotonic response of the V-population with input to the E-population (Fig. 2C H4 gray boxes indicates that negative dh_E should result in small dx_V , but positive dh_E should elicit a larger dx_V);
 We evaluate these hypotheses by taking steps in individual neuron-type input δh_α away from the modes of the inferred distributions at $y = 0.1$.

$$dh^* = z^* = \operatorname{argmax}_z \log q_\theta(z | \mathcal{B}(\alpha, 0.1)) \quad (6)$$

δx_α is the change in steady state response to the system with input $h = b + dh^* + \delta h_\alpha \hat{u}_\alpha$ compared to $h = b + dh^*$, where \hat{u}_α is a unit vector in the dimension of α . The EPI-generated hypotheses are confirmed.

H1: the neuron-type responses are sensitive to their direct inputs (Fig. 3A black, 3B blue, 3C red, 3D green);
H2: the E- and P-populations are not affected by δh_V (Fig. 3A green, 3B green);
H3: the S-population is not affected by δh_P (Fig. 3C blue);
H4: the V-population exhibits a nonmonotonic response to δh_E (Fig. 3D black), and is in fact the on population to do so (Fig. 3A-C black).

These hypotheses were in stark contrast to what was available to us via traditional analytical linear prediction (Fig. 2C, magenta). To this point, we have shown the utility of EPI on relatively low-level emergent properties like network syncing and differential neuron-type population responses. In the remainder of the study, we focus on using EPI to understand models of more abstract cognitive function.

3.4 Identifying neural mechanisms of behavioral learning.

Identifying measurable biological changes that result in improved behavior is important for neuroscience, since they may indicate how the learning brain adapts. In a rapid task switching experiment [47], rats were explicitly cued on each trial to either orient towards a visual stimulus in the Pro (P) task or orient away from a visual stimulus in the Anti (A) task (Fig. 4a). Neural recordings in the midbrain superior colliculus (SC) exhibited two populations of neurons that simultaneously represented both task context (Pro or Anti) and motor response (contralateral or ipsilateral to the recorded side): the Pro/Contra and Anti/Ipsi neurons [25]. Duan et al. proposed a model of SC that, like the V1 model analyzed in the previous section, is a four-population dynamical system. Here, the neuron-type populations are functionally-defined as the Pro- and Anti-populations in each hemisphere (left (L) and right (R)). The Pro- or Anti-populations receive an input determined by the cue, and then the left and right populations receive an input based on the side of the light stimulus. Activities were bounded between 0 and 1, so that a high output of the Pro population in a given hemisphere corresponds to the contralateral response. An additional stipulation is that when one Pro population responds with a high-output, the opposite Pro population must respond with a low output. Finally, this circuit operates in the presence of Gaussian noise resulting in trial-to-trial variability (see Section A.2.3). The connectivity matrix is parameterized by the geometry of the population arrangement (Fig. 4B).

Here, we used EPI to learn distributions of the SC weight matrix parameters $z = W$ conditioned on various levels of rapid task switching accuracy $\mathcal{B}(p)$ for $p \in \{50\%, 60\%, 70\%, 80\%, 90\%\}$ (see

276 Section A.2.3). Following the approach in Duan et al., we decomposed the connectivity matrix
 277 $W = QAQ^{-1}$ in such a way (the Schur decomposition) that the basis vectors q_i are the same for all
 278 W (Fig. 4C). These basis vectors have intuitive roles in processing for this task, and are accordingly
 279 named the *all* mode - all neurons co-fluctuate, *side* mode - one side dominates the other, *task* mode
 280 - the Pro or Anti populations dominate the other, and *diag* mode - Pro- and Anti-populations of
 281 opposite hemispheres dominate the opposite pair. The corresponding eigenvalues (e.g. a_{task} , which
 282 change according to W) indicate the degree to which activity along that mode is increased or
 283 decreased by W .

284 EPI demonstrates that, for greater task accuracies, the task mode eigenvalue increases, indicating
 285 the importance of W to the task representation (Fig. 4D, purple). Stepping from random chance
 286 (50%) networks to marginally task-performing (60%) networks, there is a marked decrease of the
 287 side mode eigenvalues (Fig. 4D, orange). Such side mode suppression remains in the models
 288 achieving greater accuracy, revealing its importance towards task performance. There were no
 289 interesting trends with learning in the all or diag mode (hence not shown in Fig. 4). Importantly,
 290 we can conclude from our methodology that side mode suppression in W allows rapid task switching,
 291 and that greater task-mode representations in W increase accuracy. These hypotheses are confirmed
 292 by forward simulation of the SC model (Fig. 4E). Thus, EPI produces novel, experimentally testable
 293 predictions: effective connectivity between these populations changes throughout learning, in a way
 294 that increases its task mode and decreases its side mode eigenvalues.

295 3.5 Linking RNN connectivity to computational error

296 So far, each model we have studied was designed from fundamental biophysical principles, genetically-
 297 or functionally-defined neuron types. At a more abstract level of modeling, recurrent neural net-
 298 works (RNNs) are high-dimensional dynamical models of computation that are becoming increas-
 299 ingly popular in neuroscience research [48]. In theoretical neuroscience, RNN dynamics usually
 300 follow the equation

$$\frac{dx(t)}{dt} = -x(t) + W\phi(x(t)) + h(t), \quad (7)$$

301 where $x(t)$ is the network activity, W is the network connectivity, $\phi(\cdot) = \tanh(\cdot)$, and $h(t)$ is the
 302 input to the system. Such RNNs are trained to do a task from a systems neuroscience experiment,
 303 and then the unit activations of the trained RNN are compared to recorded neural activity. Fully-
 304 connected RNNs with tens of thousands of parameters are challenging to characterize [49], especially
 305 making statistical inferences about their parameterization. Alternatively, we consider a rank-1, N -

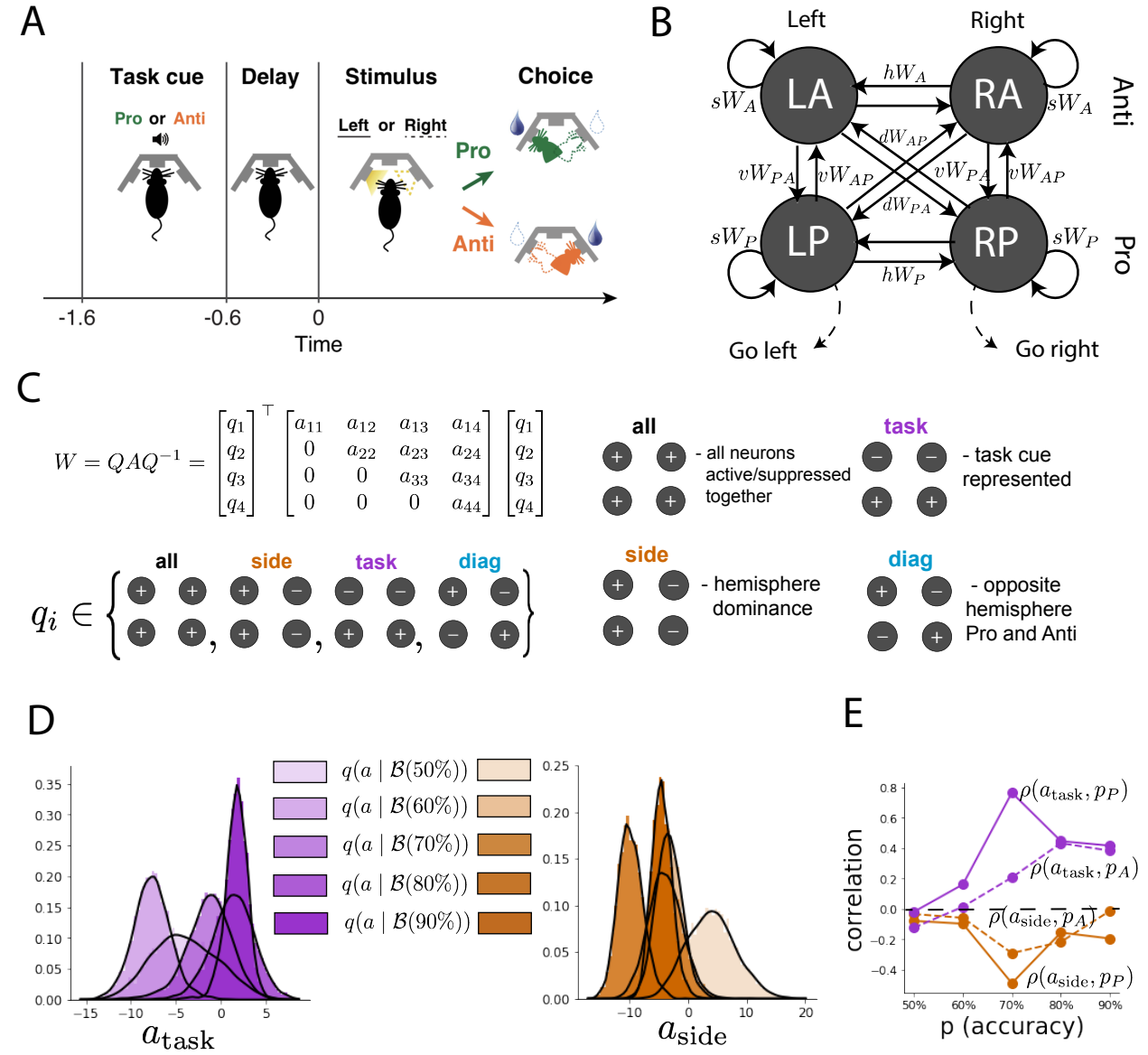


Figure 4: EPI reveals changes in SC [25] connectivity that control task accuracy. A. Rapid task switching behavioral paradigm (see text). B. Model of superior colliculus (SC). Neurons: LP - left pro, RP - right pro, LA - left anti, RA - right anti. Parameters: sW - self, hW - horizontal, vW - vertical, dW - diagonal weights. C. The Schur decomposition of the weight matrix $W = QAQ^{-1}$ is a unique decomposition with orthogonal Q and upper triangular A . Schur modes: q_{all} , q_{task} , q_{side} , and q_{diag} . D. The marginal EPI distributions of the Schur eigenvalues at each level of task accuracy. E. The correlation of Schur eigenvalue with task performance in each learned EPI distribution.

306 neuron RNN with connectivity

$$W = g\chi + \frac{1}{N}mn^\top, \quad (8)$$

307 where $\chi_{ij} \sim \mathcal{N}(0, \frac{1}{N})$, g is the random strength, and the entries of m and n are drawn from Gaussian
 308 distributions $m_i \sim \mathcal{N}(M_m, 1)$ and $n_i \sim \mathcal{N}(M_n, 1)$. We use EPI to infer the parameterizations of
 309 rank-1 RNNs solving an example task, enabling discovery of properties of connectivity that result
 310 in different types of computational errors.

311 The task we consider is Gaussian posterior conditioning: calculate the parameters of a posterior
 312 distribution induced by a prior $p(\mu_y) = \mathcal{N}(\mu_0 = 4, \sigma_0^2 = 1)$ and a likelihood $p(y|\mu_y) = \mathcal{N}(\mu_y, \sigma_y^2 =$
 313 1), given a single observation y . Conjugacy offers the result analytically; $p(\mu_y|y) = \mathcal{N}(\mu_{post}, \sigma_{post}^2)$,
 314 where:

$$\mu_{post} = \frac{\frac{\mu_0}{\sigma_0^2} + \frac{y}{\sigma_y^2}}{\frac{1}{\sigma_0^2} + \frac{1}{\sigma_y^2}} \quad \sigma_{post}^2 = \frac{1}{\frac{1}{\sigma_0^2} + \frac{1}{\sigma_y^2}}. \quad (9)$$

315 The RNN is trained to solve this task by producing readout activity that is on average the posterior
 316 mean μ_{post} , and activity whose variability is the posterior variance σ_{post}^2 (a setup inspired by
 317 [50]). To solve this Gaussian posterior conditioning task, the RNN response to a constant input
 318 $h(t) = yw + (n - M_n)$ must equal the posterior mean along readout vector r , where

$$\kappa_r = \frac{1}{N} \sum_{j=1}^N r_j \phi(x_j) \quad (10)$$

319 Additionally, the amount of chaotic variance Δ_T must equal the posterior variance. κ_r and Δ_T can
 320 be expressed in terms of each other through a solvable system of nonlinear equations (see Section
 321 A.2.4) [26]. This theory allows us to mathematically formalize the execution of this task into an
 322 emergent property, where the emergent property statistics of the RNN activity are k_r and Δ_T and
 323 the emergent property values are the ground truth posterior mean μ_{post} and variance σ_{post}^2 :

$$E \begin{bmatrix} \kappa_r \\ \Delta_T \\ (\kappa_r - \mu_{post})^2 \\ (\Delta_T^2 - \sigma_{post}^2)^2 \end{bmatrix} = \begin{bmatrix} \mu_{post} \\ \sigma_{post}^2 \\ 0.1 \\ 0.1 \end{bmatrix} \quad (11)$$

324 We specify a substantial amount of variability in the variance constraints so that the inferred
 325 distribution results in RNNs with a variety biases in their solutions to the gaussian posterior
 326 conditioning problem.

327 We used EPI to learn distributions of RNN connectivity properties $z = [g \ M_m \ M_n]$ executing
 328 Gaussian posterior conditioning given an input of $y = 2$. (see Section A.2.4) (Fig. 5B). The true

329 Gaussian conditioning posterior for an input of $y = 2$ is $\mu_{\text{post}} = 3$ and $\sigma_{\text{post}} = 0.5$. We examined
 330 the nature of the over- and under-estimation of the posterior means (Fig. 5B, left) and variances
 331 (Fig. 5B, right) in the inferred distributions. There is rough symmetry in the M_m - M_n plane,
 332 suggesting a degeneracy in the product of M_m and M_n (Fig. 5B). The product of M_m and M_n
 333 almost completely determines the posterior mean (Fig. 5B, left), and the random strength g is the
 334 most influential variable on the temporal variance (Fig. 5B, right). Neither of these observations
 335 were obvious from what mathematical analysis is available in networks of this type (see Section
 336 A.2.4). They lead to the following hypotheses:

- 337 H1: The posterior mean of the RNN increases with the product of M_m and M_n ;
 338 H2: The posterior variance increases with g ;

339

340 Testing these now in finite-size networks. Will write end of this later.

341 This novel procedure of doing inference in interpretable parameterizations of RNNs conditioned on
 342 the emergent property of task execution is straightforwardly generalizable to other tasks like noisy
 343 integration and context-dependent decision making (Fig. S1).

344 4 Discussion

345 4.1 EPI is a general tool for theoretical neuroscience

346 Models of biological systems are often comprised of complex nonlinear differential equations, mak-
 347 ing traditional theoretical analysis and statistical inference intractable. In contrast, EPI is capable
 348 of learning distributions of parameters in such models producing measurable signatures of compu-
 349 tation. We have demonstrated its utility on biological models (STG), intermediate-level models of
 350 interacting genetically- and functionally-defined neuron-types (V1, SC), and the most abstract of
 351 models (RNNs). We are able to condition both deterministic and stochastic models on low-level
 352 emergent properties like firing rates of membrane potentials, as well as high-level cognitive func-
 353 tion like Gaussian posterior conditioning. Technically, EPI is tractable when the emergent property
 354 statistics are continuously differentiable with respect to the model parameters, which is very often
 355 the case; this emphasizes the general utility of EPI.

356 In this study, we have focused on applying EPI to low dimensional parameter spaces of models
 357 with low dimensional dynamical state. These choices were made to present the reader with a series

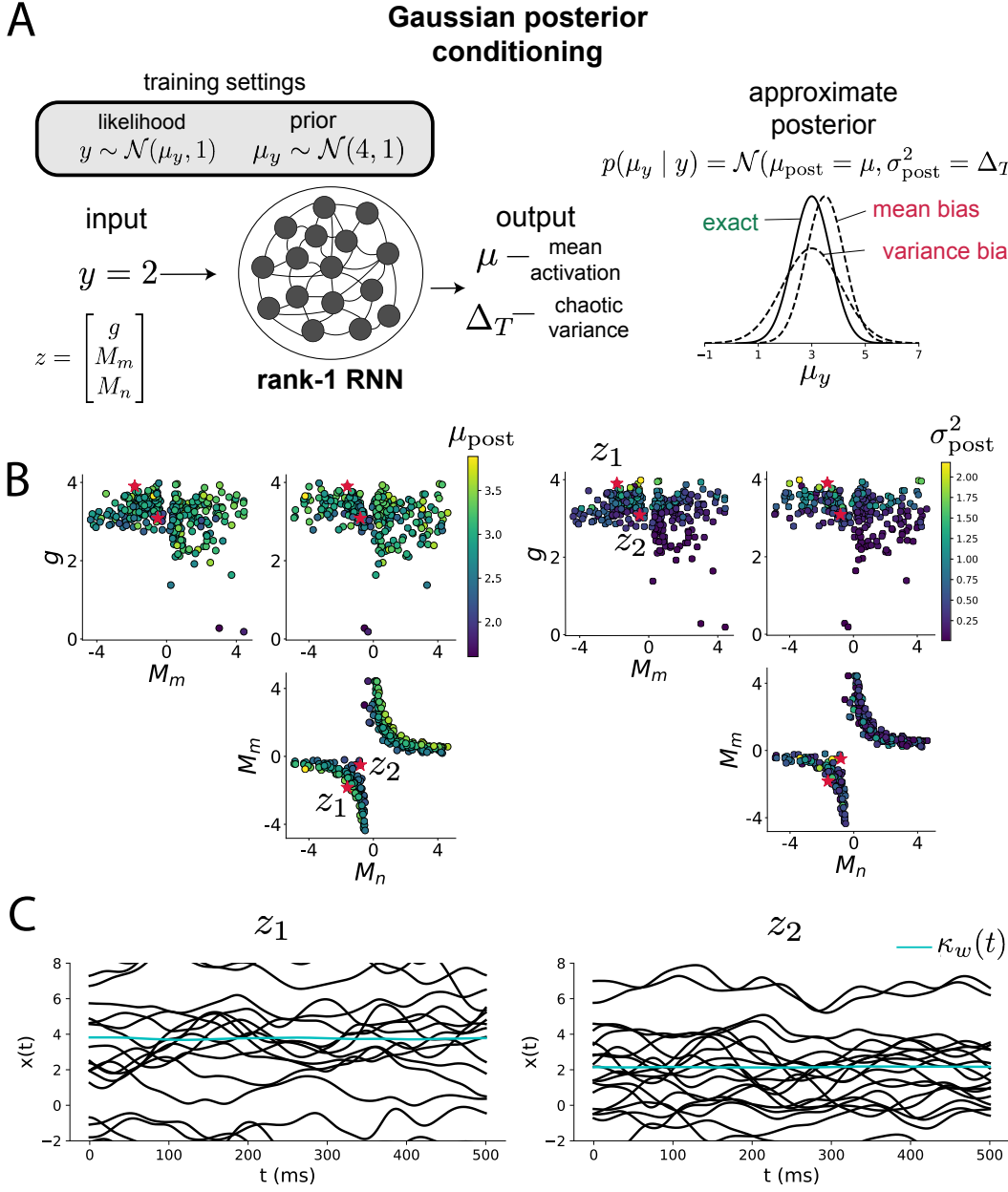


Figure 5: Sources of solution bias in an RNN computation. A. (left) A rank-1 RNN executing a Gaussian posterior conditioning computation on μ_y . (right) Bias in this computation can come from over- or under-estimating the posterior mean or variance. B. EPI distribution of rank-1 RNNs executing Gaussian posterior conditioning. Samples are colored by (left) posterior mean $\mu_{\text{post}} = \kappa_r$ and (right) posterior variance $\sigma_{\text{post}}^2 = \Delta_T$. C. Finite-size networks sampled from the distribution perform the calculation and have the computational biases expected from their parameter values. Activity along readout κ_r (cyan).

358 of interpretable conclusions, which is more challenging in high dimensional spaces. In fact, EPI
 359 should scale reasonably to high dimensional parameter spaces, as the underlying technology has
 360 produced state-of-the-art performance on high-dimensional tasks such as texture generation [20].
 361 Of course, increasing the dimensionality of the dynamical state of the model makes optimization
 362 more expensive, and there is a practical limit there as with any machine learning approach. For
 363 systems with high dimensional state, we recommend using theoretical approaches (e.g. [26]) to
 364 reason about reduced parameterizations of such high-dimensional systems.

365 There are additional technical considerations when assessing the suitability of EPI for a particu-
 366 lar modeling question. First and foremost, as in any optimization problem, the defined emergent
 367 property should always be appropriately conditioned (constraints should not have wildly different
 368 units). Furthermore, if the program is underconstrained (not enough constraints), the distribution
 369 grows (in entropy) unstably unless mapped to a finite support. If overconstrained, there is no pa-
 370 rameter set producing the emergent property, and EPI optimization will fail (appropriately). Next,
 371 one should consider the computational cost of the gradient calculations. In the best circumstance,
 372 there is a simple, closed form expression (e.g. Section A.1.1) for the emergent property statistic
 373 given the model parameters. On the other end of the spectrum, many forward simulation iterations
 374 may be required before a high quality measurement of the emergent property statistic is available
 375 (e.g. Section A.2.1). In such cases, optimization will be expensive.

376 4.2 Novel hypotheses from EPI

377 Machine learning has played an effective, multifaceted role in neuroscientific progress. Primarily,
 378 it has revealed structure in large-scale neural datasets [51, 52, 53, 54, 55, 56] (see review, [15]).
 379 Secondarily, trained algorithms of varying degrees of biological relevance are beginning to be viewed
 380 as fully-observable computational systems comparable to the brain [49, 57].

381 For example, consider the fact that we do not fully understand the four-dimensional models of V1
 382 [24]. Because analytical approaches to studying nonlinear dynamical systems become increasingly
 383 complicated when stepping from two-dimensional to three- or four-dimensional systems in the
 384 absence of restrictive simplifying assumptions [58], it is unsurprising that this model has been a
 385 challenge. In Section 3.3, we showed that EPI was far more informative about neuron-type input
 386 responsibility than the predictions afforded through analysis. By flexibly conditioning this V1 model
 387 on different emergent properties, we performed an exploratory analysis of a *model* rather than a
 388 dataset, which generated and proved out a set of testable predictions.

389 Of course, exploratory analyses can also be directed. For example, when interested in model
390 changes during learning, one can use EPI to condition as we did in Section 3.4. This analysis
391 identified experimentally testable predictions (proved out *in-silico*) of changes in connectivity in
392 SC throughout learning. Precisely, we predict that an initial reduction in side mode eigenvalue,
393 and a steady increase in task mode eigenvalue will take place, during learning, in the effective
394 connectivity matrices of learning rats.

395 In our final analysis, we present a novel procedure for doing statistical inference on interpretable
396 parameterizations of RNNs executing simple tasks . This methodology relies on recently extended
397 theory of responses in random neural networks with minimal structure [26]. With this methodology,
398 we can finally open the probabilistic model selection toolkit reasoning about the connectivity of
399 RNNs solving tasks.

400 References

- 401 [1] Larry F Abbott. Theoretical neuroscience rising. *Neuron*, 60(3):489–495, 2008.
- 402 [2] John J Hopfield. Neural networks and physical systems with emergent collective computational
403 abilities. *Proceedings of the national academy of sciences*, 79(8):2554–2558, 1982.
- 404 [3] Haim Sompolinsky, Andrea Crisanti, and Hans-Jurgen Sommers. Chaos in random neural
405 networks. *Physical review letters*, 61(3):259, 1988.
- 406 [4] Misha V Tsodyks, William E Skaggs, Terrence J Sejnowski, and Bruce L McNaughton. Para-
407 doxical effects of external modulation of inhibitory interneurons. *Journal of neuroscience*,
408 17(11):4382–4388, 1997.
- 409 [5] Kong-Fatt Wong and Xiao-Jing Wang. A recurrent network mechanism of time integration in
410 perceptual decisions. *Journal of Neuroscience*, 26(4):1314–1328, 2006.
- 411 [6] Diederik P Kingma and Max Welling. Auto-encoding variational bayes. *International Confer-
412 ence on Learning Representations*, 2014.
- 413 [7] Danilo Jimenez Rezende, Shakir Mohamed, and Daan Wierstra. Stochastic backpropagation
414 and variational inference in deep latent gaussian models. *International Conference on Machine
415 Learning*, 2014.

- [8] Yuanjun Gao, Evan W Archer, Liam Paninski, and John P Cunningham. Linear dynamical neural population models through nonlinear embeddings. In *Advances in neural information processing systems*, pages 163–171, 2016.
- [9] Yuan Zhao and Il Memming Park. Recursive variational bayesian dual estimation for nonlinear dynamics and non-gaussian observations. *stat*, 1050:27, 2017.
- [10] Gabriel Barello, Adam Charles, and Jonathan Pillow. Sparse-coding variational auto-encoders. *bioRxiv*, page 399246, 2018.
- [11] Chethan Pandarinath, Daniel J O’Shea, Jasmine Collins, Rafal Jozefowicz, Sergey D Stavisky, Jonathan C Kao, Eric M Trautmann, Matthew T Kaufman, Stephen I Ryu, Leigh R Hochberg, et al. Inferring single-trial neural population dynamics using sequential auto-encoders. *Nature methods*, page 1, 2018.
- [12] Alexander B Wiltschko, Matthew J Johnson, Giuliano Iurilli, Ralph E Peterson, Jesse M Katon, Stan L Pashkovski, Victoria E Abraira, Ryan P Adams, and Sandeep Robert Datta. Mapping sub-second structure in mouse behavior. *Neuron*, 88(6):1121–1135, 2015.
- [13] Matthew J Johnson, David K Duvenaud, Alex Wiltschko, Ryan P Adams, and Sandeep R Datta. Composing graphical models with neural networks for structured representations and fast inference. In *Advances in neural information processing systems*, pages 2946–2954, 2016.
- [14] Eleanor Batty, Matthew Whiteway, Shreya Saxena, Dan Biderman, Taiga Abe, Simon Musall, Winthrop Gillis, Jeffrey Markowitz, Anne Churchland, John Cunningham, et al. Behavenet: nonlinear embedding and bayesian neural decoding of behavioral videos. *Advances in Neural Information Processing Systems*, 2019.
- [15] Liam Paninski and John P Cunningham. Neural data science: accelerating the experiment-analysis-theory cycle in large-scale neuroscience. *Current opinion in neurobiology*, 50:232–241, 2018.
- [16] Mark K Transtrum, Benjamin B Machta, Kevin S Brown, Bryan C Daniels, Christopher R Myers, and James P Sethna. Perspective: Sloppiness and emergent theories in physics, biology, and beyond. *The Journal of chemical physics*, 143(1):07B201_1, 2015.
- [17] Danilo Jimenez Rezende and Shakir Mohamed. Variational inference with normalizing flows. *International Conference on Machine Learning*, 2015.

- [445] [18] Laurent Dinh, Jascha Sohl-Dickstein, and Samy Bengio. Density estimation using real nvp.
[446] *arXiv preprint arXiv:1605.08803*, 2016.
- [447] [19] George Papamakarios, Theo Pavlakou, and Iain Murray. Masked autoregressive flow for density
[448] estimation. In *Advances in Neural Information Processing Systems*, pages 2338–2347, 2017.
- [449] [20] Gabriel Loaiza-Ganem, Yuanjun Gao, and John P Cunningham. Maximum entropy flow
[450] networks. *International Conference on Learning Representations*, 2017.
- [451] [21] Dustin Tran, Rajesh Ranganath, and David Blei. Hierarchical implicit models and likelihood-
[452] free variational inference. In *Advances in Neural Information Processing Systems*, pages 5523–
[453] 5533, 2017.
- [454] [22] Mark S Goldman, Jorge Golowasch, Eve Marder, and LF Abbott. Global structure, robustness,
[455] and modulation of neuronal models. *Journal of Neuroscience*, 21(14):5229–5238, 2001.
- [456] [23] Gabrielle J Gutierrez, Timothy O’Leary, and Eve Marder. Multiple mechanisms switch an
[457] electrically coupled, synaptically inhibited neuron between competing rhythmic oscillators.
[458] *Neuron*, 77(5):845–858, 2013.
- [459] [24] Ashok Litwin-Kumar, Robert Rosenbaum, and Brent Doiron. Inhibitory stabilization and vi-
[460] sual coding in cortical circuits with multiple interneuron subtypes. *Journal of neurophysiology*,
[461] 115(3):1399–1409, 2016.
- [462] [25] Chunyu A Duan, Marino Pagan, Alex T Piet, Charles D Kopec, Athena Akrami, Alexander J
[463] Riordan, Jeffrey C Erlich, and Carlos D Brody. Collicular circuits for flexible sensorimotor
[464] routing. *bioRxiv*, page 245613, 2018.
- [465] [26] Francesca Mastrogiovanni and Srdjan Ostojic. Linking connectivity, dynamics, and computa-
[466] tions in low-rank recurrent neural networks. *Neuron*, 99(3):609–623, 2018.
- [467] [27] Sean R Bittner, Agostina Palmigiano, Kenneth D Miller, and John P Cunningham. Degener-
[468] ate solution networks for theoretical neuroscience. *Computational and Systems Neuroscience
[469] Meeting (COSYNE), Lisbon, Portugal*, 2019.
- [470] [28] Sean R Bittner, Alex T Piet, Chunyu A Duan, Agostina Palmigiano, Kenneth D Miller,
[471] Carlos D Brody, and John P Cunningham. Examining models in theoretical neuroscience with
[472] degenerate solution networks. *Bernstein Conference*, 2019.

- 473 [29] Jan-Matthis Lueckmann, Pedro Goncalves, Chaitanya Chintaluri, William F Podlaski, Giacomo Bassetto, Tim P Vogels, and Jakob H Macke. Amortised inference for mechanistic models
474 of neural dynamics. In *Computational and Systems Neuroscience Meeting (COSYNE), Lisbon, Portugal*, 2019.
- 477 [30] Jan-Matthis Lueckmann, Pedro J Goncalves, Giacomo Bassetto, Kaan Öcal, Marcel Nonnenmacher, and Jakob H Macke. Flexible statistical inference for mechanistic models of neural
478 dynamics. In *Advances in Neural Information Processing Systems*, pages 1289–1299, 2017.
- 480 [31] Eve Marder and Vatsala Thirumalai. Cellular, synaptic and network effects of neuromodulation. *Neural Networks*, 15(4-6):479–493, 2002.
- 482 [32] Astrid A Prinz, Dirk Bucher, and Eve Marder. Similar network activity from disparate circuit
483 parameters. *Nature neuroscience*, 7(12):1345, 2004.
- 484 [33] Edwin T Jaynes. Information theory and statistical mechanics. *Physical review*, 106(4):620,
485 1957.
- 486 [34] Gamaleldin F Elsayed and John P Cunningham. Structure in neural population recordings:
487 an expected byproduct of simpler phenomena? *Nature neuroscience*, 20(9):1310, 2017.
- 488 [35] Cristina Savin and Gašper Tkačik. Maximum entropy models as a tool for building precise
489 neural controls. *Current opinion in neurobiology*, 46:120–126, 2017.
- 490 [36] Brendan K Murphy and Kenneth D Miller. Balanced amplification: a new mechanism of
491 selective amplification of neural activity patterns. *Neuron*, 61(4):635–648, 2009.
- 492 [37] Hirofumi Ozeki, Ian M Finn, Evan S Schaffer, Kenneth D Miller, and David Ferster. Inhibitory
493 stabilization of the cortical network underlies visual surround suppression. *Neuron*, 62(4):578–
494 592, 2009.
- 495 [38] Daniel B Rubin, Stephen D Van Hooser, and Kenneth D Miller. The stabilized supralinear
496 network: a unifying circuit motif underlying multi-input integration in sensory cortex. *Neuron*,
497 85(2):402–417, 2015.
- 498 [39] Henry Markram, Maria Toledo-Rodriguez, Yun Wang, Anirudh Gupta, Gilad Silberberg, and
499 Caizhi Wu. Interneurons of the neocortical inhibitory system. *Nature reviews neuroscience*,
500 5(10):793, 2004.

- 501 [40] Bernardo Rudy, Gordon Fishell, SooHyun Lee, and Jens Hjerling-Leffler. Three groups of
502 interneurons account for nearly 100% of neocortical gabaergic neurons. *Developmental neuro-*
503 *biology*, 71(1):45–61, 2011.
- 504 [41] Robin Tremblay, Soohyun Lee, and Bernardo Rudy. GABAergic Interneurons in the Neocortex:
505 From Cellular Properties to Circuits. *Neuron*, 91(2):260–292, 2016.
- 506 [42] Carsten K Pfeffer, Mingshan Xue, Miao He, Z Josh Huang, and Massimo Scanziani. Inhi-
507 bition of inhibition in visual cortex: the logic of connections between molecularly distinct
508 interneurons. *Nature Neuroscience*, 16(8):1068, 2013.
- 509 [43] Luis Carlos Garcia Del Molino, Guangyu Robert Yang, Jorge F. Mejias, and Xiao Jing Wang.
510 Paradoxical response reversal of top- down modulation in cortical circuits with three interneu-
511 ron types. *Elife*, 6:1–15, 2017.
- 512 [44] Guang Chen, Carl Van Vreeswijk, David Hansel, and David Hansel. Mechanisms underlying
513 the response of mouse cortical networks to optogenetic manipulation. 2019.
- 514 [45] (2018) Allen Institute for Brain Science. Layer 4 model of v1. available from:
515 <https://portal.brain-map.org/explore/models/l4-mv1>.
- 516 [46] Yazan N Billeh, Binghuang Cai, Sergey L Gratiy, Kael Dai, Ramakrishnan Iyer, Nathan W
517 Gouwens, Reza Abbasi-Asl, Xiaoxuan Jia, Joshua H Siegle, Shawn R Olsen, et al. Systematic
518 integration of structural and functional data into multi-scale models of mouse primary visual
519 cortex. *bioRxiv*, page 662189, 2019.
- 520 [47] Chunyu A Duan, Jeffrey C Erlich, and Carlos D Brody. Requirement of prefrontal and midbrain
521 regions for rapid executive control of behavior in the rat. *Neuron*, 86(6):1491–1503, 2015.
- 522 [48] Omri Barak. Recurrent neural networks as versatile tools of neuroscience research. *Current*
523 *opinion in neurobiology*, 46:1–6, 2017.
- 524 [49] David Sussillo and Omri Barak. Opening the black box: low-dimensional dynamics in high-
525 dimensional recurrent neural networks. *Neural computation*, 25(3):626–649, 2013.
- 526 [50] Rodrigo Echeveste, Laurence Aitchison, Guillaume Hennequin, and Máté Lengyel. Cortical-like
527 dynamics in recurrent circuits optimized for sampling-based probabilistic inference. *bioRxiv*,
528 page 696088, 2019.

- 529 [51] Robert E Kass and Valérie Ventura. A spike-train probability model. *Neural computation*,
530 13(8):1713–1720, 2001.
- 531 [52] Emery N Brown, Loren M Frank, Dengda Tang, Michael C Quirk, and Matthew A Wilson.
532 A statistical paradigm for neural spike train decoding applied to position prediction from
533 ensemble firing patterns of rat hippocampal place cells. *Journal of Neuroscience*, 18(18):7411–
534 7425, 1998.
- 535 [53] Liam Paninski. Maximum likelihood estimation of cascade point-process neural encoding
536 models. *Network: Computation in Neural Systems*, 15(4):243–262, 2004.
- 537 [54] M Yu Byron, John P Cunningham, Gopal Santhanam, Stephen I Ryu, Krishna V Shenoy, and
538 Maneesh Sahani. Gaussian-process factor analysis for low-dimensional single-trial analysis
539 of neural population activity. In *Advances in neural information processing systems*, pages
540 1881–1888, 2009.
- 541 [55] Kenneth W Latimer, Jacob L Yates, Miriam LR Meister, Alexander C Huk, and Jonathan W
542 Pillow. Single-trial spike trains in parietal cortex reveal discrete steps during decision-making.
543 *Science*, 349(6244):184–187, 2015.
- 544 [56] Lea Duncker, Gergo Bohner, Julien Boussard, and Maneesh Sahani. Learning interpretable
545 continuous-time models of latent stochastic dynamical systems. *Proceedings of the 36th Inter-*
546 *national Conference on Machine Learning*, 2019.
- 547 [57] Blake A Richards and et al. A deep learning framework for neuroscience. *Nature Neuroscience*,
548 2019.
- 549 [58] Steven H Strogatz. Nonlinear dynamics and chaos: with applications to physics. *Biology,*
550 *Chemistry, and Engineering (Studies in Nonlinearity)*, Perseus, Cambridge, UK, 1994.
- 551 [59] Rajesh Ranganath, Sean Gerrish, and David Blei. Black box variational inference. In *Artificial*
552 *Intelligence and Statistics*, pages 814–822, 2014.
- 553 [60] Martin J Wainwright, Michael I Jordan, et al. Graphical models, exponential families, and
554 variational inference. *Foundations and Trends® in Machine Learning*, 1(1–2):1–305, 2008.
- 555 [61] Laurent Dinh, Jascha Sohl-Dickstein, and Samy Bengio. Density estimation using real nvp.
556 *Proceedings of the 5th International Conference on Learning Representations*, 2017.

557 **A Methods**

558 **A.1 Emergent property inference (EPI)**

559 Emergent property inference (EPI) learns distributions of theoretical model parameters that pro-
 560 duce emergent properties of interest. EPI combines ideas from likelihood-free variational inference
 561 [21] and maximum entropy flow networks [20]. A maximum entropy flow network is used as a deep
 562 probability distribution for the parameters, while these samples often parameterize a differentiable
 563 model simulator, which may lack a tractable likelihood function.

564 Consider model parameterization z and data x generated from some theoretical model simulator
 565 represented as $p(x | z)$, which may be deterministic or stochastic. Theoretical models usually have
 566 known sampling procedures for simulating activity given a circuit parameterization, yet often lack
 567 an explicit likelihood function due to the nonlinearities and dynamics. With EPI, a distribution
 568 on parameters z is learned, that yields an emergent property of interest \mathcal{B} ,

$$\mathcal{B} \triangleq \mathbb{E}_{z \sim q_\theta} [\mathbb{E}_{x \sim p(x|z)} [T(x)]] = \mu \quad (12)$$

569 by making an approximation $q_\theta(z)$ to $p(z | \mathcal{B})$ (see Section A.1.5). So, over the DSN distribution
 570 $q_\theta(z)$ of model $p(x | z)$ for behavior \mathcal{B} , the emergent properties $T(x)$ are constrained in expectation
 571 to μ .

572 In deep probability distributions, a simple random variable $w \sim q_0$ is mapped deterministically via
 573 a function f_θ parameterized by a neural network to the support of the distribution of interest where
 574 $z = f_\theta(w) = f_l(\dots f_1(w))$. Given a theoretical model $p(x | z)$ and some behavior of interest \mathcal{B} , the
 575 deep probability distributions are trained by optimizing the neural network parameters θ to find a
 576 good approximation q_θ^* within the deep variational family \mathcal{Q} to $p(z | \mathcal{B})$.

577 In most settings (especially those relevant to theoretical neuroscience) the likelihood of the behavior
 578 with respect to the model parameters $p(T(x) | z)$ is unknown or intractable, requiring an alternative
 579 to stochastic gradient variational Bayes [6] or black box variational inference[59]. These types
 580 of methods called likelihood-free variational inference (LFVI, [21]) skate around the intractable
 581 likelihood function in situations where there is a differentiable simulator. Akin to LFVI, DSNs are
 582 optimized with the following objective for a given theoretical model, emergent property statistics
 583 $T(x)$, and emergent property constraints μ :

$$\begin{aligned} q_\theta^*(z) &= \operatorname{argmax}_{q_\theta \in Q} H(q_\theta(z)) \\ \text{s.t. } \mathbb{E}_{z \sim q_\theta} [\mathbb{E}_{x \sim p(x|z)} [T(x)]] &= \mu \end{aligned} \tag{13}$$

584 Optimizing this objective is a technological accomplishment in its own right, the details of which
 585 we elaborate in Section A.1.2. Before going through those details, we ground this optimization in
 586 a toy example.

587 **A.1.1 Example: 2D LDS**

588 To gain intuition for EPI, consider two-dimensional linear dynamical systems, $\tau \dot{x} = Ax$ with

$$A = \begin{bmatrix} a_1 & a_2 \\ a_3 & a_4 \end{bmatrix}$$

589 that produce a band of oscillations. To do EPI with the dynamics matrix elements as the free
 590 parameters $z = [a_1, a_2, a_3, a_4]$, and fixing $\tau = 1$, such that the posterior yields a band of oscillations,
 591 the emergent property statistics $T(x)$ are chosen to contain the first- and second-moments of the
 592 oscillatory frequency ω and the growth/decay factor d of the oscillating system. To learn the
 593 distribution of real entries of A that yield a distribution of d with mean zero with variance 0.25^2 ,
 594 and oscillation frequency ω with mean 1 Hz with variance $(0.1\text{Hz})^2$, then we would select the real
 595 part of the complex conjugate eigenvalues $\operatorname{real}(\lambda_1) = d$ (via an arbitrary choice of eigenvalue of the
 596 dynamics matrix λ_1) and the positive imaginary component of one of the eigenvalues $\operatorname{imag}(\lambda_1) =$
 597 $2\pi\omega$ as the emergent property statistics. Those emergent property statistics are then constrained
 598 to

$$\mu = \mathbb{E} \begin{bmatrix} \operatorname{real}(\lambda_1) \\ \operatorname{imag}(\lambda_1) \\ (\operatorname{real}(\lambda_1) - 0)^2 \\ (\operatorname{imag}(\lambda_1) - 2\pi\omega)^2 \end{bmatrix} = \begin{bmatrix} 0.0 \\ 2\pi\omega \\ 0.25^2 \\ (2\pi 0.1)^2 \end{bmatrix} \tag{14}$$

599 where $\omega = 1\text{Hz}$. Unlike the models we study in the paper which calculate $\mathbb{E}_{x \sim p(x|z)} [T(x)]$ via
 600 forward simulation, we have a closed form for the eigenvalues of the dynamics matrix. λ can be
 601 calculated using the quadratic formula:

$$\lambda = \frac{\left(\frac{a_1+a_4}{\tau}\right) \pm \sqrt{\left(\frac{a_1+a_4}{\tau}\right)^2 + 4\left(\frac{a_2a_3-a_1a_4}{\tau}\right)}}{2} \tag{15}$$



Fig. S2: A. Two-dimensional linear dynamical system model, where real entries of the dynamics matrix A are the parameters. B. The DSN distribution for a 2D LDS with $\tau = 1$ that produces an average of 1Hz oscillations with some small amount of variance. C. Entropy throughout the optimization. At the beginning of each augmented Lagrangian epoch (5,000 iterations), the entropy dips due to the shifted optimization manifold where emergent property constraint satisfaction is increasingly weighted. D. Emergent property moments throughout optimization. At the beginning of each augmented Lagrangian epoch, the emergent property moments move closer to their constraints.

602 where λ_1 is the eigenvalue of $\frac{1}{\tau}A$ with greatest real part. Even though $\mathbb{E}_{x \sim p(x|z)}[T(x)]$ is calculable
 603 directly via a closed form function and does not require simulation, we cannot derive the distribution
 604 q_θ^* directly. This is due to the formally hard problem of the backward mapping: finding the natural
 605 parameters η from the mean parameters μ of an exponential family distribution [60]. Instead, we
 606 can use EPI to learn the linear system parameters producing such a band of oscillations (Fig. S2B).
 607 Even this relatively simple system has nontrivial (though intuitively sensible) structure in the
 608 parameter distribution. To validate our method (further than that of the underlying technology
 609 on a ground truth solution [20]) we can analytically derive the contours of the probability density
 610 from the emergent property statistics and values (Fig. S3). In the $a_1 - a_4$ plane, is a black line
 611 at $\text{real}(\lambda_1) = \frac{a_1+a_4}{2} = 0$, a dotted black line at the standard deviation $\text{real}(\lambda_1) = \frac{a_1+a_4}{2} \pm 1$, and a
 612 grey line at twice the standard deviation $\text{real}(\lambda_1) = \frac{a_1+a_4}{2} \pm 2$ (Fig. S3A). Here the lines denote the
 613 set of solutions at fixed behaviors, which overlay the posterior obtained through EPI. The learned
 614 DSN distribution precisely reflects the desired statistical constraints and model degeneracy in the
 615 sum of a_1 and a_4 . Intuitively, the parameters equivalent with respect to emergent property statistic
 616 $\text{real}(\lambda_1)$ have similar log densities.

617 To explain the structure in the bimodality of the DSN posterior, we can look at the imaginary
 618 component of λ_1 . When $\text{real}(\lambda_1) = \frac{a_1+a_4}{2} = 0$, we have

$$\text{imag}(\lambda_1) = \begin{cases} \sqrt{\frac{a_1a_4-a_2a_3}{\tau}}, & \text{if } a_1a_4 < a_2a_3 \\ 0 & \text{otherwise} \end{cases} \quad (16)$$

619 When $\tau = 1$ and $a_1a_4 > a_2a_3$ (center of distribution above), we have the following equation for the
 620 other two dimensions:

$$\text{imag}(\lambda_1)^2 = a_1a_4 - a_2a_3 \quad (17)$$

621 Since we constrained $\mathbb{E}_{z \sim q_\theta}[\text{imag}(\lambda)] = 2\pi$ (with $\omega = 1$), we can plot contours of the equation
 622 $\text{imag}(\lambda_1)^2 = a_1a_4 - a_2a_3 = (2\pi)^2$ for various a_1a_4 (Fig. S3A). If $\sigma_{1,4} = \mathbb{E}_{z \sim q_\theta}(|a_1a_4 - E_{q_\theta}[a_1a_4]|)$,
 623 then we plot the contours as $a_1a_4 = 0$ (black), $a_1a_4 = -\sigma_{1,4}$ (black dotted), and $a_1a_4 = -2\sigma_{1,4}$
 624 (grey dotted) (Fig. S3B). This validates the curved structure of the inferred distribution learned
 625 through EPI. We take steps in negative standard deviation of a_1a_4 (dotted and gray lines), since
 626 there are few positive values a_1a_4 in the posterior. Subtler model-behavior combinations will have
 627 even more complexity, further motivating the use of EPI for understanding these systems. Indeed,
 628 we sample a distribution of systems oscillating near 1Hz (Fig. S4).

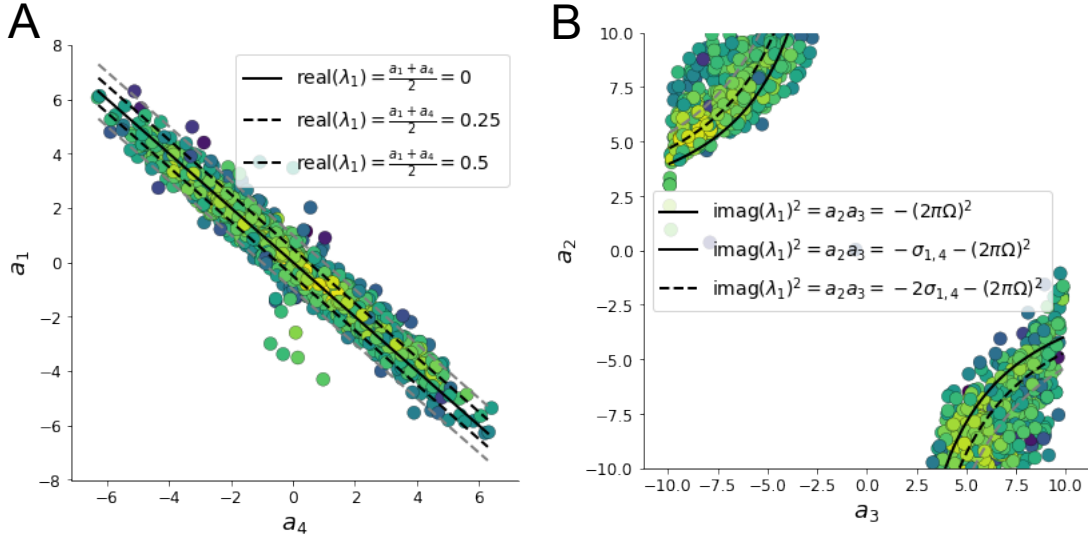


Fig. S3: A. Probability contours in the $a_1 - a_4$ plane can be derived from the relationship to emergent property statistic of growth/decay factor. B. Probability contours in the $a_2 - a_3$ plane can be derived from relationship to the emergent property statistic of oscillation frequency.

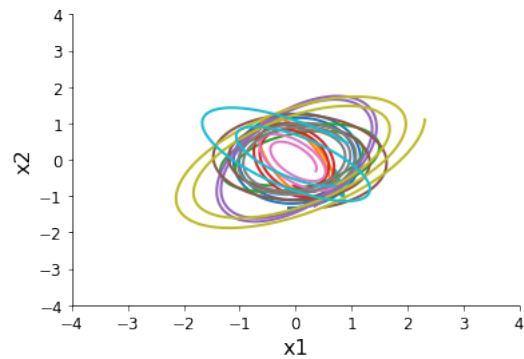


Fig. S4: Sampled dynamical system trajectories from the EPI distribution. Each trajectory is initialized at $x(0) = \left[\frac{\sqrt{2}}{2} \quad -\frac{\sqrt{2}}{2} \right]$.

629 **A.1.2 Augmented Lagrangian optimization**

630 To optimize $q_\theta(z)$ in Equation 13, the constrained optimization is performed using the augmented
 631 Lagrangian method. The following objective is minimized:

$$L(\theta; \eta, c) = -H(q_\theta) + \eta^\top R(\theta) + \frac{c}{2} \|R(\theta)\|^2 \quad (18)$$

632 where $R(\theta) = \mathbb{E}_{z \sim q_\theta} [\mathbb{E}_{x \sim p(x|z)} [T(x) - \mu]]$, $\eta \in \mathbb{R}^m$ are the Lagrange multipliers and c is the penalty
 633 coefficient. For a fixed (η, c) , θ is optimized with stochastic gradient descent. A low value of c is
 634 used initially, and increased during each augmented Lagrangian epoch – a period of optimization
 635 with fixed η and c for a given number of stochastic optimization iterations. Similarly, η is tuned
 636 each epoch based on the constraint violations. For the linear 2-dimensional system (Fig. S2C)
 637 optimization hyperparameters are initialized to $c_1 = 10^{-4}$ and $\eta_1 = \mathbf{0}$. The penalty coefficient
 638 is updated based on a hypothesis test regarding the reduction in constraint violation. The p-
 639 value of $E[\|R(\theta_{k+1})\|] > \gamma \mathbb{E}[\|R(\theta_k)\|]$ is computed, and c_{k+1} is updated to βc_k with probability
 640 $1 - p$. Throughout the project, $\beta = 4.0$ and $\gamma = 0.25$ is used. The other update rule is $\eta_{k+1} =$
 641 $\eta_k + c_k \frac{1}{n} \sum_{i=1}^n (T(x^{(i)}) - \mu)$. In this example, each augmented Lagrangian epoch ran for 2,000
 642 iterations. We consider the optimization to have converged when a null hypothesis test of constraint
 643 violations being zero is accepted for all constraints at a significance threshold 0.05. This is the dotted
 644 line on the plots below depicting the optimization cutoff of EPI optimization for the 2-dimensional
 645 linear system. If the optimization is left to continue running, entropy usually decreases, and
 646 structural pathologies in the distribution may be introduced.

647 The intention is that c and η start at values encouraging entropic growth early in optimization.
 648 Then, as they increase in magnitude with each training epoch, the constraint satisfaction terms are
 649 increasingly weighted, resulting in a decrease in entropy. Rather than using a naive initialization,
 650 before EPI, we optimize the deep probability distribution parameters to generate samples of an
 651 isotropic Gaussian of a selected variance, such as 1.0 for the 2D LDS example. This provides a
 652 convenient starting point, whose level of entropy is controlled by the user.

653 **A.1.3 Normalizing flows**

654 Since we are optimizing parameters θ of our deep probability distribution with respect to the
 655 entropy, we will need to take gradients with respect to the log-density of samples from the deep
 656 probability distribution.

$$H(q_\theta(z)) = \int -q_\theta(z) \log(q_\theta(z)) dz = \mathbb{E}_{z \sim q_\theta} [-\log(q_\theta(z))] = \mathbb{E}_{w \sim q_0} [-\log(q_\theta(f_\theta(w)))] \quad (19)$$

$$\nabla_\theta H(q_\theta(z)) = \mathbb{E}_{w \sim q_0} [-\nabla_\theta \log(q_\theta(f_\theta(w)))] \quad (20)$$

Deep probability models typically consist of several layers of fully connected neural networks. When each neural network layer is restricted to be a bijective function, the sample density can be calculated using the change of variables formula at each layer of the network. For $z' = f(z)$,

$$q(z') = q(f^{-1}(z')) \left| \det \frac{\partial f^{-1}(z')}{\partial z'} \right| = q(z) \left| \det \frac{\partial f(z)}{\partial z} \right|^{-1} \quad (21)$$

However, this computation has cubic complexity in dimensionality for fully connected layers. By restricting our layers to normalizing flows [17] – bijective functions with fast log determinant jacobian computations, we can tractably optimize deep generative models with objectives that are a function of sample density, like entropy. Most of our analyses use real NVP [61], which have proven effective in our architecture searches, and have the advantageous features of fast sampling and fast density evaluation.

A.1.4 Related work

(To come)

669

A.1.5 Emergent property inference as variational inference in an exponential family

(To come)

672

A.2 Theoretical models

In this study, we used emergent property inference to examine several models relevant to theoretical neuroscience. Here, we provide the details of each model and the related analyses.

676 **A.2.1 Stomatogastric ganglion**

677 Each neuron's membrane potential $x_m(t)$ is the solution of the following differential equation.

$$C_m \frac{dx_m}{dt} = -[h_{leak}(x; z) + h_{Ca}(x; z) + h_K(x; z) + h_{hyp}(x; z) + h_{elec}(x; z) + h_{syn}(x; z)] \quad (22)$$

678 The membrane potential of each neuron is affected by the leak, calcium, potassium, hyperpolariza-
 679 tion, electrical and synaptic currents, respectively. The capacitance of the cell membrane was set to
 680 $C_m = 1nF$. Each current is a function of the neuron's membrane potential x_m and the parameters
 681 of the circuit such as g_{el} and g_{syn} , whose effect on the circuit is considered in the motivational
 682 example of EPI in Fig. 1. Specifically, the currents are the difference in the neuron's membrane
 683 potential and that current type's reversal potential multiplied by a conductance:

$$h_{leak}(x; z) = g_{leak}(x_m - V_{leak}) \quad (23)$$

$$h_{elec}(x; z) = g_{el}(x_m^{post} - x_m^{pre}) \quad (24)$$

$$h_{syn}(x; z) = g_{syn}S_\infty^{pre}(x_m^{post} - V_{syn}) \quad (25)$$

$$h_{Ca}(x; z) = g_{Ca}M_\infty(x_m - V_{Ca}) \quad (26)$$

$$h_K(x; z) = g_KN(x_m - V_K) \quad (27)$$

$$h_{hyp}(x; z) = g_hH(x_m - V_{hyp}) \quad (28)$$

689 The reversal potentials were set to $V_{leak} = -40mV$, $V_{Ca} = 100mV$, $V_K = -80mV$, $V_{hyp} = -20mV$,
 690 and $V_{syn} = -75mV$. The other conductance parameters were fixed to $g_{leak} = 1 \times 10^{-4}\mu S$. g_{Ca} ,
 691 g_K , and g_{hyp} had different values based on fast, intermediate (hub) or slow neuron. Fast: $g_{Ca} =$
 692 1.9×10^{-2} , $g_K = 3.9 \times 10^{-2}$, and $g_{hyp} = 2.5 \times 10^{-2}$. Intermediate: $g_{Ca} = 1.7 \times 10^{-2}$, $g_K = 1.9 \times 10^{-2}$,
 693 and $g_{hyp} = 8.0 \times 10^{-3}$. Intermediate: $g_{Ca} = 8.5 \times 10^{-3}$, $g_K = 1.5 \times 10^{-2}$, and $g_{hyp} = 1.0 \times 10^{-2}$.

694 Furthermore, the Calcium, Potassium, and hyperpolarization channels have time-dependent gating
 695 dynamics dependent on steady-state gating variables M_∞ , N_∞ and H_∞ , respectively.

$$M_\infty = 0.5 \left(1 + \tanh \left(\frac{x_m - v_1}{v_2} \right) \right) \quad (29)$$

$$\frac{dN}{dt} = \lambda_N(N_\infty - N) \quad (30)$$

$$N_\infty = 0.5 \left(1 + \tanh \left(\frac{x_m - v_3}{v_4} \right) \right) \quad (31)$$

$$\lambda_N = \phi_N \cosh \left(\frac{x_m - v_3}{2v_4} \right) \quad (32)$$

699

$$\frac{dH}{dt} = \frac{(H_\infty - H)}{\tau_h} \quad (33)$$

700

$$H_\infty = \frac{1}{1 + \exp\left(\frac{x_m + v_5}{v_6}\right)} \quad (34)$$

701

$$\tau_h = 272 - \left(\frac{-1499}{1 + \exp\left(\frac{-x_m + v_7}{v_8}\right)} \right) \quad (35)$$

702 where we set $v_1 = 0mV$, $v_2 = 20mV$, $v_3 = 0mV$, $v_4 = 15mV$, $v_5 = 78.3mV$, $v_6 = 10.5mV$,
 703 $v_7 = -42.2mV$, $v_8 = 87.3mV$, $v_9 = 5mV$, and $v_{th} = -25mV$. These are the same parameter
 704 values used in [23].

705 Finally, there is a synaptic gating variable as well:

$$S_\infty = \frac{1}{1 + \exp\left(\frac{v_{th} - x_m}{v_9}\right)} \quad (36)$$

706 When the dynamic gating variables are considered, this is actually a 15-dimensional nonlinear
 707 dynamical system.

708 In order to measure the frequency of the hub neuron during EPI, the STG model was simulated
 709 for $T = 500$ time steps of $dt = 25ms$. In EPI, since gradients are taken through the simulation
 710 process, the number of time steps are kept as modest if possible. The chosen dt and T were the
 711 most computationally convenient choices yielding accurate frequency measurement.

712 Our original approach to measuring frequency was to take the max of the fast Fourier transform
 713 (FFT) of the simulated time series. There are a few key considerations here. One is resolution
 714 in frequency space. Each FFT entry will correspond to a signal frequency of $\frac{F_s k}{N}$, where N is
 715 the number of samples used for the FFT, $F_s = \frac{1}{dt}$, and $k \in [0, 1, \dots, N - 1]$. Our resolution is
 716 improved by increasing N and decreasing dt . Increasing $N = T - b$, where b is some fixed number
 717 of buffer burn-in initialization samples, necessitates an increase in simulation time steps T , which
 718 directly increases computational cost. Increasing F_s (decreasing dt) increases system approximation
 719 accuracy, but requires more time steps before a full cycle is observed. At the level of $dt = 0.025$,
 720 thousands of temporal samples were required for resolution of .01Hz. These challenges in frequency
 721 resolution with the discrete Fourier transform motivated the use of an alternative basis of complex
 722 exponentials. Instead, we used a basis of complex exponentials with frequencies from 0.0-1.0 Hz at
 723 0.01Hz resolution, $\Phi = [0.0, 0.01, \dots, 1.0]^\top$

724 Another consideration was that the frequency spectra of the hub neuron has several peaks. This
 725 was due to high-frequency sub-threshold activity. The maximum frequency was often not the firing

frequency. Accordingly, subthreshold activity was set to zero, and the whole signal was low-pass filtered with a moving average window of length 20. The signal was subsequently mean centered. After this pre-processing, the maximum frequency in the filter bank accurately reflected the firing frequency.

Finally, to differentiate through the maximum frequency identification step, we used a sum-of-powers normalization strategy: Let $\mathcal{X}_i \in \mathcal{C}^{|\Phi|}$ be the complex exponential filter bank dot products with the signal $x_i \in \mathbb{R}^N$, where $i \in \{\text{f1}, \text{f2}, \text{hub}, \text{s1}, \text{s2}\}$. The “frequency identification” vector is

$$u_i = \frac{|\mathcal{X}_i|^\alpha}{\sum_{k=1}^N |\mathcal{X}_i(k)|^\alpha} \quad (37)$$

The frequency is then calculated as $\omega = u_i^\top \Phi$ with $\alpha = 100$.

Network syncing, like all other emergent properties in this work, are defined by the emergent property statistics and values. The emergent property statistics are the first- and second-moments of the firing frequencies. The first moments are set to 0.542Hz, while the second moments are set to 0.025Hz².

$$E \begin{bmatrix} \omega_{\text{f1}} \\ \omega_{\text{f2}} \\ \omega_{\text{hub}} \\ \omega_{\text{s1}} \\ \omega_{\text{s2}} \\ (\omega_{\text{f1}} - 0.542)^2 \\ (\omega_{\text{f2}} - 0.542)^2 \\ (\omega_{\text{hub}} - 0.542)^2 \\ (\omega_{\text{s1}} - 0.542)^2 \\ (\omega_{\text{s2}} - 0.542)^2 \end{bmatrix} = \begin{bmatrix} 0.542 \\ 0.542 \\ 0.542 \\ 0.542 \\ 0.542 \\ 0.025^2 \\ 0.025^2 \\ 0.025^2 \\ 0.025^2 \\ 0.025^2 \end{bmatrix} \quad (38)$$

For EPI in Fig 2C, we used a real NVP architecture with two coupling layers. Each coupling layer had two hidden layers of 10 units each, and we mapped onto a support of $z \in \left[\begin{bmatrix} 0 \\ 0 \end{bmatrix}, \begin{bmatrix} 10 \\ 8 \end{bmatrix} \right]$. We have shown the EPI optimization that converged with maximum entropy across 2 random seeds and augmented Lagrangian coefficient initializations of $c_0=0$, 2, and 5.

742 **A.2.2 Primary visual cortex**743 The dynamics of each neural populations average rate $x = \begin{bmatrix} x_E \\ x_P \\ x_S \\ x_V \end{bmatrix}$ are given by:

$$\tau \frac{dx}{dt} = -x + [Wx + h]_+^n \quad (39)$$

744 Some neuron-types largely lack synaptic projections to other neuron-types [42], and it is popular

745 to only consider a subset of the effective connectivities [24].

$$W = \begin{bmatrix} W_{EE} & W_{EP} & W_{ES} & 0 \\ W_{PE} & W_{PP} & W_{PS} & 0 \\ W_{SE} & 0 & 0 & W_{SV} \\ W_{VE} & W_{VP} & W_{VS} & 0 \end{bmatrix} \quad (40)$$

746 By consolidating information from many experimental datasets, Billeh et al. [46] produce estimates

747 of the synaptic strength (in mV)

$$M = \begin{bmatrix} 0.36 & 0.48 & 0.31 & 0.28 \\ 1.49 & 0.68 & 0.50 & 0.18 \\ 0.86 & 0.42 & 0.15 & 0.32 \\ 1.31 & 0.41 & 0.52 & 0.37 \end{bmatrix} \quad (41)$$

748 and connection probability

$$C = \begin{bmatrix} 0.16 & 0.411 & 0.424 & 0.087 \\ 0.395 & .451 & 0.857 & 0.02 \\ 0.182 & 0.03 & 0.082 & 0.625 \\ 0.105 & 0.22 & 0.77 & 0.028 \end{bmatrix} \quad (42)$$

749 Multiplying these connection probabilities and synaptic efficacies gives us an effective connectivity

750 matrix:

$$W_{\text{full}} = C \odot M = \begin{bmatrix} 0.16 & 0.411 & 0.424 & 0.087 \\ 0.395 & .451 & 0.857 & 0.02 \\ 0.182 & 0.03 & 0.082 & 0.625 \\ 0.105 & 0.22 & 0.77 & 0.028 \end{bmatrix} \quad (43)$$

751 From use the entries of this full effective connectivity matrix that are not considered to be ineffectual.

753 We look at how this four-dimensional nonlinear dynamical model of V1 responds to different inputs,
 754 and compare the predictions of the linear response to the approximate posteriors obtained through
 755 EPI. The input to the system is the sum of a baseline input $b = [1 \ 1 \ 1 \ 1]^\top$ and a differential
 756 input dh :

$$h = b + dh \quad (44)$$

757 All simulations of this system had $T = 100$ time points, a time step $dt = 5\text{ms}$, and time constant
 758 $\tau = 20\text{ms}$. And the system was initialized to a random draw $x(0)_i \sim \mathcal{N}(1, 0.01)$.

759 We can describe the dynamics of this system more generally by

$$\dot{x}_i = -x_i + f(u_i) \quad (45)$$

760 where the input to each neuron is

$$u_i = \sum_j W_{ij}x_j + h_i \quad (46)$$

761 Let $F_{ij} = \gamma_i \delta(i, j)$, where $\gamma_i = f'(u_i)$. Then, the linear response is

$$\frac{dx_{ss}}{dh} = F(W \frac{dx_{ss}}{dh} + I) \quad (47)$$

762 which is calculable by

$$\frac{dx_{ss}}{dh} = (F^{-1} - W)^{-1} \quad (48)$$

763 The emergent property we considered was the first and second moments of the change in rate dx
 764 between the baseline input $h = b$ and $h = b + dh$. We use the following notation to indicate that
 765 the emergent property statistics were set to the following values:

$$\mathcal{B}(\alpha, y) \triangleq \mathbb{E} \begin{bmatrix} dx_{\alpha,ss} \\ (dx_{\alpha,ss} - y)^2 \end{bmatrix} = \begin{bmatrix} y \\ 0.01^2 \end{bmatrix} \quad (49)$$

766 In the final analysis for this model, we sweep the input one neuron at a time away from the mode
 767 of each inferred distributions $dh^* = z^* = \text{argmax}_z \log q_\theta(z \mid \mathcal{B}(\alpha, 0.1))$. The differential responses
 768 $\delta x_{\alpha,ss}$ are examined at perturbed inputs $h = b + dh^* + \delta h_\alpha \hat{u}_\alpha$ where \hat{u}_α is a unit vector in the
 769 dimension of α and $\delta h_\alpha \in [-15, 15]$.

770 For each $\mathcal{B}(\alpha, y)$ with $\alpha \in \{E, P, S, V\}$ and $y \in \{0.1, 0.5\}$, we ran EPI with five different random
 771 initial seeds using an architecture of four coupling layers, each with two hidden layers of 10 units.

772 We set $c_0 = 10^5$. The support of the learned distribution was restricted to $z_i \in [-5, 5]$.

773 **A.2.3 Superior colliculus**

774 In the model of Duan et al [25], there are four total units: two in each hemisphere corresponding to
 775 the Pro/Contra and Anti/Ipsi populations. They are denoted as left Pro (LP), left Anti (LA), right
 776 Pro (RP) and right Anti (RA). Each unit has an activity (x_α) and internal variable (u_α) related
 777 by

$$x_\alpha(t) = \left(\frac{1}{2} \tanh \left(\frac{u_\alpha(t) - \epsilon}{\zeta} \right) + \frac{1}{2} \right) \quad (50)$$

778 where $\alpha \in \{LP, LA, RA, RP\}$. $\epsilon = 0.05$ and $\zeta = 0.5$ control the position and shape of the nonlin-
 779 earity, respectively.

780 We order the elements of x and u in the following manner

$$x = \begin{bmatrix} x_{LP} \\ x_{LA} \\ x_{RP} \\ x_{RA} \end{bmatrix} \quad u = \begin{bmatrix} u_{LP} \\ u_{LA} \\ u_{RP} \\ u_{RA} \end{bmatrix} \quad (51)$$

781 The internal variables follow dynamics:

$$\tau \frac{dv}{dt} = -u + Wx + h + \sigma dB \quad (52)$$

782 with time constant $\tau = 0.09s$ and Gaussian noise σdB controlled by the magnitude of $\sigma = 1.0$. The
 783 weight matrix has 8 parameters sW_P , sW_A , vW_{PA} , vW_{AP} , hW_P , hW_A , dW_{PA} , and dW_{AP} (Fig.
 784 4B).

$$W = \begin{bmatrix} sW_P & vW_{PA} & hW_P & dW_{PA} \\ vW_{AP} & sW_A & dW_{AP} & hW_A \\ hW_P & dW_{PA} & sW_P & vW_{PA} \\ dW_{AP} & hW_A & vW_{AP} & sW_A \end{bmatrix} \quad (53)$$

785 The system receives five inputs throughout each trial, which has a total length of 1.8s.

$$h = h_{\text{rule}} + h_{\text{choice-period}} + h_{\text{light}} \quad (54)$$

786 There are rule-based inputs depending on the condition,

$$h_{P,\text{rule}}(t) = \begin{cases} I_{P,\text{rule}} \begin{bmatrix} 1 & 0 & 0 & 1 \end{bmatrix}^\top, & \text{if } t \leq 1.2s \\ 0, & \text{otherwise} \end{cases} \quad (55)$$

787

$$h_{A,\text{rule}}(t) = \begin{cases} I_{A,\text{rule}} \begin{bmatrix} 0 & 1 & 1 & 0 \end{bmatrix}^\top, & \text{if } t \leq 1.2s \\ 0, & \text{otherwise} \end{cases} \quad (56)$$

788 a choice-period input,

$$h_{\text{choice}}(t) = \begin{cases} I_{\text{choice}} \begin{bmatrix} 1 & 1 & 1 & 1 \end{bmatrix}^\top, & \text{if } t > 1.2s \\ 0, & \text{otherwise} \end{cases} \quad (57)$$

789 and an input to the right or left-side depending on where the light stimulus is delivered.

$$h_{\text{light}}(t) = \begin{cases} I_{\text{light}} \begin{bmatrix} 1 & 1 & 0 & 0 \end{bmatrix}^\top, & \text{if } t > 1.2s \text{ and Left} \\ I_{\text{light}} \begin{bmatrix} 0 & 0 & 1 & 1 \end{bmatrix}^\top, & \text{if } t > 1.2s \text{ and Right} \\ 0, & t \leq 1.2s \end{cases} \quad (58)$$

790 The input parameterization was fixed to $I_{P,\text{rule}} = 10$, $I_{A,\text{rule}} = 10$, $I_{\text{choice}} = 2$, and $I_{\text{light}} = 1$ 791 To produce a Bernoulli rate of p_{LP} in the Left, Pro condition (we can generalize this to either cue,
792 or stimulus condition), let \hat{p}_i be the empirical average steady state (ss) response (final x_{LP} at end
793 of task) over $M=500$ Gaussian noise draws for a given SC model parameterization z_i :

$$\hat{p}_i = \mathbb{E}_{\sigma dB} [x_{LP} | s = L, c = P, z_i] = \frac{1}{M} \sum_{j=1}^M x_{LP}(s = L, c = P, z_i, \sigma dB_j) \quad (59)$$

794 where here x_α denotes the steady state activity at the end of the trial. For the first constraint, the
795 average over posterior samples (from $q_\theta(z)$) to be p_{LP} :

$$\mathbb{E}_{z_i \sim q_\phi} [\mathbb{E}_{\sigma dB} [x_{LP,ss} | s = L, c = P, z_i]] = \mathbb{E}_{z_i \sim q_\phi} [\hat{p}_i] = p_{LP} \quad (60)$$

796 We can then ask that the variance of the steady state responses across Gaussian draws, is the
797 Bernoulli variance for the empirical rate \hat{p}_i .

$$\mathbb{E}_{z \sim q_\phi} [\sigma_{err}^2] = 0 \quad (61)$$

798

$$\sigma_{err}^2 = Var_{\sigma dB} [x_{LP} | s = L, c = P, z_i] - \hat{p}_i(1 - \hat{p}_i) \quad (62)$$

799 We have an additional constraint that the Pro neuron on the opposite hemisphere should have the
800 opposite value. We can enforce this with a final constraint:

$$\mathbb{E}_{z \sim q_\phi} [d_P] = 1 \quad (63)$$

801

$$\mathbb{E}_{\sigma dB} [(x_{LP} - x_{RP})^2 \mid s = L, c = P, z_i] \quad (64)$$

802 We refer to networks obeying these constraints as Bernoulli, winner-take-all networks. Since the
 803 maximum variance of a random variable bounded from 0 to 1 is the Bernoulli variance ($\hat{p}(1 - \hat{p})$),
 804 and the maximum squared difference between two variables bounded from 0 to 1 is 1, we do not
 805 need to control the second moment of these test statistics. In reality, these variables are dynamical
 806 system states and can only exponentially decay (or saturate) to 0 (or 1), so the Bernoulli variance
 807 error and squared difference constraints can only be undershot. This is important to be mindful
 808 of when evaluating the convergence criteria. Instead of using our usual hypothesis testing criteria
 809 for convergence to the emergent property, we set a slack variable threshold for these technically
 810 infeasible constraints to 0.05.

811 Training DSNs to learn distributions of dynamical system parameterizations that produce Bernoulli
 812 responses at a given rate (with small variance around that rate) was harder to do than expected.
 813 There is a pathology in this optimization setup, where the learned distribution of weights is bimodal
 814 attributing a fraction p of the samples to an expansive mode (which always sends x_{LP} to 1), and a
 815 fraction $1 - p$ to a decaying mode (which always sends x_{LP} to 0). This pathology was avoided using
 816 an inequality constraint prohibiting parameter samples that resulted in low variance of responses
 817 across noise.

818 In total, the emergent property of rapid task switching accuracy at level p was defined as

$$\mathcal{B}(p) \triangleq \begin{bmatrix} \hat{p}_P \\ \hat{p}_A \\ (\hat{p}_P - p)^2 \\ (\hat{p}_A - p)^2 \\ \sigma_{P,err}^2 \\ \sigma_{A,err}^2 \\ d_P \\ d_A \end{bmatrix} = \begin{bmatrix} p \\ p \\ 0.15^2 \\ 0.15^2 \\ 0 \\ 0 \\ 1 \\ 1 \end{bmatrix} \quad (65)$$

819 For each accuracy level p , we ran EPI for 10 different random seeds and selected the maximum
 820 entropy solution using an architecture of 10 planar flows with $c_0 = 2$. The support of z was \mathbb{R}^8 . s

821 **A.2.4 Rank-1 RNN**

822 Recent work establishes a link between RNN connectivity weights and the resulting dynamical
 823 responses of the network, using dynamic mean field theory (DMFT) [26]. Specifically, DMFT
 824 describes the properties of activity in infinite-size neural networks given a distribution on the
 825 connectivity weights. In such a model, the connectivity of a rank-1 RNN (which was sufficient for
 826 our task), has weight matrix W , which is the sum of a random component with strength determined
 827 by g and a structured component determined by the outer product of vectors m and n :

$$W = g\chi + \frac{1}{N}mn^\top, \quad (66)$$

828 where the activity x evolves as $\dot{x} = I(t)$ and $I(t)$ is some input, ϕ is the tanh nonlinearity, and $\chi_{ij} \sim \mathcal{N}(0, \frac{1}{N})$.
 829 The entries of m and n are drawn from Gaussian distributions $m_i \sim \mathcal{N}(M_m, 1)$ and $n_i \sim \mathcal{N}(M_n, 1)$.
 830 From such a parameterization, this theory produces consistency equations for the dynamic mean
 831 field variables in terms of parameters like g , M_m , and M_n , which we study in Section 3.5. That
 832 is the dynamic mean field variables (e.g. the activity along a vector κ_v , the total variance
 833 Δ_0 , structured variance Δ_∞ , and the chaotic variance Δ_T) are written as functions of one another
 834 in terms of connectivity parameters. The values of these variables can be obtained using a
 835 nonlinear system of equations solver. These dynamic mean field variables are then cast as task-
 836 relevant variables with respect to the context of the provided inputs. Mastrogiuseppe et al. designed
 837 low-rank RNN connectivities via minimalist connectivity parameters to solve canonical tasks from
 838 behavioral neuroscience.

839 We consider the DMFT equation solver as a black box that takes in a low-rank parameterization
 840 z (e.g. $z = [g \ M_m \ M_n]$) and outputs the values of the dynamic mean field variables, of which
 841 we cast κ_r and Δ_T as task-relevant variables μ_{post} and σ_{post}^2 in the Gaussian posterior conditioning
 842 toy example. Importantly, the solution produced by the solver is differentiable with respect to the
 843 input parameters, allowing us to use DMFT to calculate the emergent property statistics in EPI
 844 to learn distributions on such connectivity parameters of RNNs that execute tasks.

845 Specifically, we solve for the mean field variables κ_r , κ_n , Δ_0 and Δ_∞ , where the readout is nominally
 846 chosen to point in the unit orthant $r = [1 \ \dots \ 1]^\top$. The consistency equations for these variables

847 in the presence of a constant input $h(t) = y - (n - M_n)$ can be derived following [26] are

$$\begin{aligned}\kappa_r &= G_1(\kappa_r, \kappa_n, \Delta_0, \Delta_\infty) = M_m \kappa_n + y \\ \kappa_n &= G_2(\kappa_r, \kappa_n, \Delta_0, \Delta_\infty) = M_n \langle [\phi_i] \rangle + \langle [\phi'_i] \rangle \\ \frac{\Delta_0^2 - \Delta_\infty^2}{2} &= G_3(\kappa_r, \kappa_n, \Delta_0, \Delta_\infty) = g^2 \left(\int \mathcal{D}z \Phi^2 (\kappa_r + \sqrt{\Delta_0} z) - \int \mathcal{D}z \int \mathcal{D}x \Phi (\kappa_r + \sqrt{\Delta_0 - \Delta_\infty} x + \sqrt{\Delta_\infty} z) \right) \\ &\quad + (\kappa_n^2 + 1)(\Delta_0 - \Delta_\infty) \\ \Delta_\infty &= G_4(\kappa_r, \kappa_n, \Delta_0, \Delta_\infty) = g^2 \int \mathcal{D}z \left[\int \mathcal{D}x \phi (\kappa_r + \sqrt{\Delta_0 - \Delta_\infty} x + \sqrt{\Delta_\infty} z) \right]^2 + \kappa_n^2 + 1\end{aligned}\tag{67}$$

848 where z here is a gaussian integration variable. We can solve these equations by simulating the
849 following Langevin dynamical system to a steady state.

$$\begin{aligned}l(t) &= \frac{\Delta_0(t)^2 - \Delta_\infty(t)^2}{2} \\ \Delta_0(t) &= \sqrt{2x(t) + \Delta_\infty(t)^2} \\ \frac{d\kappa_r(t)}{dt} &= -\kappa_r(t) + F(\kappa_r(t), \kappa_n(t), \Delta_0(t), \Delta_\infty(t)) \\ \frac{d\kappa_n(t)}{dt} &= -\kappa_n + G(\kappa_r(t), \kappa_n(t), \Delta_0(t), \Delta_\infty(t)) \\ \frac{dI(t)}{dt} &= -l(t) + H(\kappa_r(t), \kappa_n(t), \Delta_0(t), \Delta_\infty(t)) \\ \frac{d\Delta_\infty(t)}{dt} &= -\Delta_\infty(t) + L(\kappa_r(t), \kappa_n(t), \Delta_0(t), \Delta_\infty(t))\end{aligned}\tag{68}$$

850 Then, the chaotic variance, which is necessary for the Gaussian posterior conditioning example, is
851 simply calculated via

$$\Delta_T = \Delta_0 - \Delta_\infty\tag{69}$$

852 A.3 Supplementary Figures

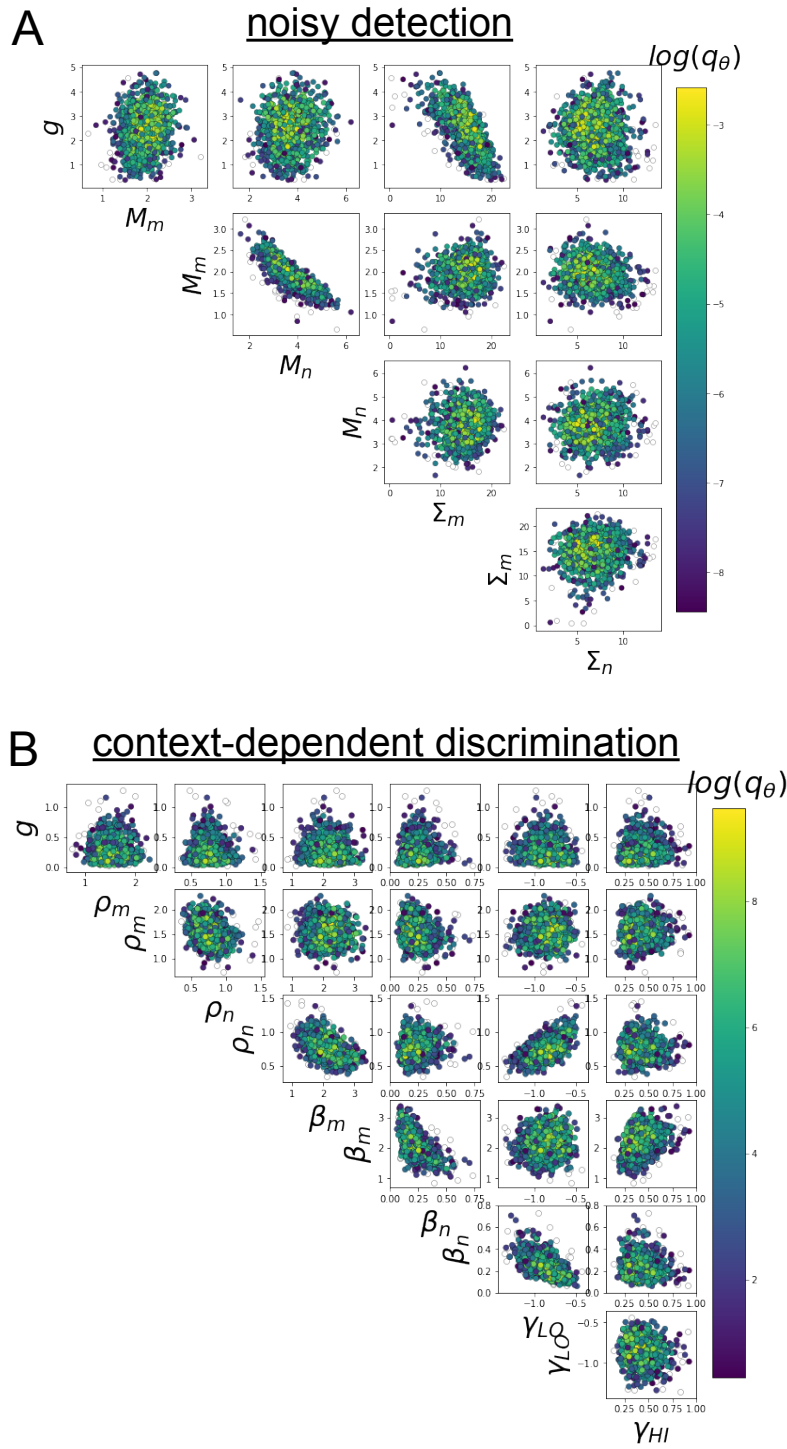


Fig. S1: A. EPI for rank-1 networks doing discrimination. B. EPI for rank-2 networks doing context-dependent discrimination.